Progress in Warm Liquid Calorimetry at PENN and Request for Interim Funding

Robert Hollebeek
Charles Katz
Mitch Newcomer
Michael Gregory
University of Pennsylvania

August 22, 1990

Ionization Calorimeters

The direct collection of ionization produced in electromagnetic and hadronic calorimeters has been used for many years in high energy physics. Examples include calorimeters using primarily liquid Argon or Xenon for sampling, the liquified noble gases being chosen to eliminate absorption of the direct ionization by the sampling medium. This technology has now been used in many recent large detectors including Mark II, SLD, and D0.

In most of the examples to date, the motivation for using this technique has been a combination of two factors; calibration stability and ease of segmentation in the construction of the calorimeter. The good calibration stability of these devices comes about because the direct ionization yield in the detector depends only on fixed properties of the liquid (i.e. density, Z, de/dx etc.) The detector's calibration scale is therefore very stable. Of course, care must be taken to ensure that the liquid remains pure, and that the amplifier gains can be calibrated with direct charge injection; problems which have been shown to be solvable on a large scale in present detectors. Eliminated in this technique are the problems of variable quantum efficiency, spectral shifts, phototube gain variation, non-uniform light collection, sampling medium aging or radiation damage and other problems which affect techniques which rely on indirect measurements of calorimeter ionization.

Small segmentation in a calorimeter is important for electron identification, jet invariant mass measurement, detection of leptons close to a jet, heavy quark isolation requirements, and pileup rejection. Often the desire to employ small segmentation in the design of a calorimeter must be mediated by the realities of mechanical design or by the relative cost of more electronics or readout channels. Relative to scintillator techniques however, liquid ionization has very little problem accommodating both the longitudinal and transverse segmentation requirements encountered in conceptual SSC detector designs.

Increased segmentation can become difficult to achieve when the extra room needed to get the signal out of a device is a significant fraction of the size of the calorimeter segment. An obvious point in favor of liquid ionization devices is that the mechanical space taken up in the design by the extra wire required for a new channel in a ionization device is small compared to the space taken by wave guides, light shifters, and even fiber readout in a scintillator design. In contrast to many current designs for calorimeters utilizing scintillators and/or fibers, longitudinal segmentation is not a problem for liquid ionization devices. This gives added confidence that the calorimeter electron identification will not be compromised. The cost of the additional electronics needed to support longitudinal segmentation is reasonable.

In summary, what started out 15 years ago as a difficult technology (liquid Argon detectors)

involving as much art as science in the purification of noble gases and the construction of detectors, has progressed to a relatively standard and well understood technique with good prospects for extension to SSC scale calorimeters. Experience has shown however that two major draw-backs may continue to hinder the use of this technique. The first problem is that since the noble gas sampling medium lacks hydrogen, conversion of some of the hadronic energy flow carried by neutrons (a relatively large fraction of the total energy flow with significant fluctuations and hence significant contributions to the resolution) via slow neutron collisions which produce slow (but highly ionizing) protons, is missing. The presence of this effect is now believed to be important in determining the ultimate resolution of a hadron calorimeter. Calorimeters which do have this mechanism are called "compensating" which refers to the balance between the yield expected for electromagnetic and hadronic shower components. Since the typical hadronic shower itself contains both electromagnetic (π^0) and hadronic components with large fluctuations between the two, this balance is important for the optimization of the calorimeter resolution. Tests have now shown that by adjusting the sampling medium thickness or composition so that this balance is achieved, the resolution can be improved by as much as factors of two to three over calorimeters built in the past with typically $100\%/\sqrt{E}$ hadronic resolution.

A further problem encountered in recent ionization calorimeters has been the need for a cryogenic envelope around the calorimeter with consequent difficulties in designing a calorimeter with complete coverage. As physics focuses more and more on weak interaction physics involving W and Z production as well as future signatures for W', Z', supersymmetry, Higgs, top etc., the desire both to maintain adequate missing energy resolution for $W \rightarrow e\nu, \mu\nu, \tau\nu$ signatures as well as to reconstruct or at least constrain W and Z decays into hadronic channels becomes increasingly important. The need to provide cryogenic isolation for the calorimeter in the case of liquid noble gases conflicts directly with these desires because the vacuum vessel introduces significant dead space into the design which in turn affects both the overall calorimeter resolution and the missing energy resolution. This problem becomes particularly difficult for most detectors in the region between the central calorimeter and the plug or end cap region. The introduction of a magnet into the design makes the problem all the more complex. The most recent example, D0, paid particular attention to this problem, but nevertheless has significant material in the region $0.8 \leq |\eta| \leq 1.2$ which is right in the middle of the range important for lepton, W, and Z detection from heavy sources ($|\eta| \leq 2.$) Attempts to improve the situation by using chambers in front of these problem regions (i.e. crack chambers) have been made both in conceptual designs (Liquid Argon SSC designs) and in present detectors (CDF). Experience with CDF has shown however that these regions are typically ignored in physics analysis because the loss in resolution, increase in systematics, and increased analysis problems tend to be so great as to not be worth the minor increase in acceptance. Nevertheless, the lost acceptance can be relatively more important for multi-body final states containing for example 4-leptons (an interesting Higgs signature) or multi-jets (for W signatures).

Room Temperature Ionization Calorimetry

By replacing the ionization medium used in the calorimeter with a material which is a liquid at room temperature, all of the advantages of liquid calorimetry can be retained while eliminating many of the difficulties. Several candidate liquids have been known now for a few years thanks primarily to the efforts of the UA1 group at CERN. The most attractive liquid is TMS or Tetra Methyl Silane. It is a very spherical molecule with a tetrahedral arrangement of four methyl (CH_3) groups surrounding a silicon atom. Silanes are chemical compounds which have silicon replacing carbon and are used as surficants, inerting compounds, biological implants, bonding agents and many other uses. TMS is the first by-product in the production of silanes, and is available in very large quantities. Its primary usage is in minute quantities used in NMR spectroscopy (its 12 fold degenerate C-H bond defines the zero for NMR).

The major draw back to TMS is shared by all of the other candidate compounds and that is

its flammability. Because of the risk of a Uranium fire in the UA1 calorimeter which is situated in close proximity to a populated area (Meyrin), the UA1 group chose to use TMP (tetra Methyl Pentane) $4(CH_3)\ C_2$ instead of TMS. The disadvantage of TMP is that it has a lower drift velocity. The faster drift velocity in TMS is important for SSC detectors and results in a factor of 2-3 improvement in signal to noise for fixed measurement and shaping times relative to TMP. Minor additional advantages of TMS relative to TMP and other candidate liquids include the ability of the gas phase to withstand high electric fields without breakdown (due to the high vapor pressure) and ease of purification (due to low boiling point relative to common contaminants).

The recent problems encountered by the UA1 collaboration in their attempts to produce the first large scale TMP hadron calorimeter have been the subject of many discussions among physicists. The problems include production delays with the boxes used to isolate the liquid from the reused metal in the old gondolas, low yield for HV feed thrus and high voltage breakdown within some of the constructed modules. None of these problems appear to be due to fundamental problems with liquids themselves, most are related to the detailed design of the boxes used to contain the liquid. The HV breakdown problem was not seen in prototype modules, and is now believed to be due to contaminants introduced during the filling procedure.

Because of the UA1 experience with the difficulty of producing the liquid containment boxes, and because of the difficulty of extrapolating the "box per gap" calorimeter design to SSC-scale hadron calorimeters, more recent efforts in warm liquid calorimetry have focused on what is now known as a "swimming pool" design in which the metal radiators are immersed directly in the liquid. This is in fact what is always done in liquid Argon detectors. In this approach, increased care needs to be taken in the selection of materials for the calorimeter construction since more of these materials come into direct contact with the liquid itself.

PENN Warm Liquid Program

At Penn, we have concentrated on the use of TMS because of the significant advantages which it offers in the construction and operation of the calorimeter if the safety problems can be solved. The greatest advantage is due directly to the fast drift velocity, which makes this detector one of the fastest radiation-hard, compensating detectors known. The primary goals of our research have been:

1. to develop diagnostic tools which can determine the degree of contamination of liquid samples and identify the contaminants
2. to investigate the available purification techniques, determine which are most effective, and simplify the process so that one can economically produce large volumes of liquid
3. to test the compatibility of the liquid with materials to be used in calorimeter construction.

The most important accomplishments to date have been

1. demonstration of the feasibility of operating TMS in the presence of lead plates made from typical calorimeter lead and treated with simple cleaning procedures
2. development of the use of mass spectrometry as a diagnostic monitor of the container cleanliness during and after filling
3. simplification of the cleaning procedures for TMS with the demonstration of lifetimes seven times the drift time for a two step purification scheme
4. detection of contaminants in TMS using a dual detector gas chromatograph and the beginning of a chemical calibration library for the columns used
5. first operation of a detector stack using electrostatic readout in a warm liquid

6. demonstration of liquid compatibility for materials used in the test beam module (TBM) construction including lead, kapton, resistors, and connectors.

The purification setup which we have constructed at Penn is presently used for TMS, but is general enough to handle other liquids including liquid Argon in small quantities. A diagram of the system is shown in figure 1. The vacuum pump is a turbomolecular pump which is used because it pumps heavy molecules with high speed, and it is a clean pump in the sense that there is very little backstreaming of heavy compounds. A large gate valve isolates the pump from the rest of the system when necessary. The system has several types of vacuum gauges including thermocouple gauges, a cold cathode gauge and an ionization gauge which reads down to about 10^{-11}. The system regularly pumps to less than 10^{-7}. The primary tool for determining the quality of the vacuum and the cleanliness of the system is the residual gas analyzer. This device is a quadropole mass-spectrometer with a resolution of about 0.1 atomic mass units. It is used both to determine the cleanliness of the containers after bakeout or pumping and to analyze samples as they are purified or samples from the detectors. TMS spectra from this device are shown in figure 2. The spectrum has a small peak at mass 88 which is the molecular weight of TMS. The strongest peak is 73 which corresponds to the loss of one methyl group. Isotopic abundance ratios of the peaks can be used to recognize the contributions from TMS and other compounds particularly because of the characteristic values of these abundances for Silicon.

Inlet samples of gases, TMS, residual contaminants from the purification procedures and gas phase from the detectors can now be sent to a gas chromatograph which has just been installed in the last few months. A sample trace from a TMS sample is shown in figure 3. The trace (which comes from a flame ionization detector FID) shows that the TMS from the vendor is 99.96% pure but contains as many as six other compounds. An extensive library of retention times for various chemicals using the column is being developed in order to identify these contaminants. One of these compounds was at first identified as Toluene based on its retention time, but has since been shown to be some other unknown compound. The gas chromatograph has two parallel detectors: the FID and an electron capture device. This latter detector consists of a large radioactive Nickel source and an ionization detector, and can therefore measure directly the absorption of electrons by the contaminants. In this way, we hope to be able to separate out those contaminants which affect the electron lifetime in the detector from those which do not so that we can concentrate on the former.

During the past year, we have been using three detectors (see figure 4). The first is a 16 gap stainless steel stack with 1.6mm gaps. This is the third in a series of such modules and contains some materials (copper, macor, silver solder connections) which have been determined not to significantly affect electron lifetime in previous tests. This module is used as a normalization module. The input capacitance of the stack is about 120pf.

The second detector is a 10 gap stack of 5x5 cm lead plates, each 1/4 in thick. The stack is constructed form lead-antimony alloy used for construction of liquid argon modules. A similar detector has 10x10cm plates which gives it roughly the size and input capacitance of an SSC hadronic calorimeter tower. These detectors were the first ones to demonstrate the feasibility of operating a detector with TMS in direct contact with lead plates. The cleaning procedure used for the plates has been a standard chemical wash sequence using high megohm water, acetone and alcohol. Auger surface analysis of lead plates treated in this way has since shown that the surface is as clean as is usually achieved with baked stainless steel.

Both detectors have had the liquid in contact with the plates for long enough to measure the time dependence of the charge yield from the TMS. The yield for the larger detector as a function of time is shown in figure 5. Similar behavior has been demonstrated for several batches of liquid. Since it has been shown with this series of tests that it is possible to achieve reasonable charge yield in this configuration, it is possible to contemplate calorimeter designs for TMS and TMP which are quite similar in their construction techniques to those used in liquid argon detectors.

A fourth detector (1x1) has just recently been installed. It is a prototype of the construction techniques to be used in the full TBM and includes several new materials in the construction. The

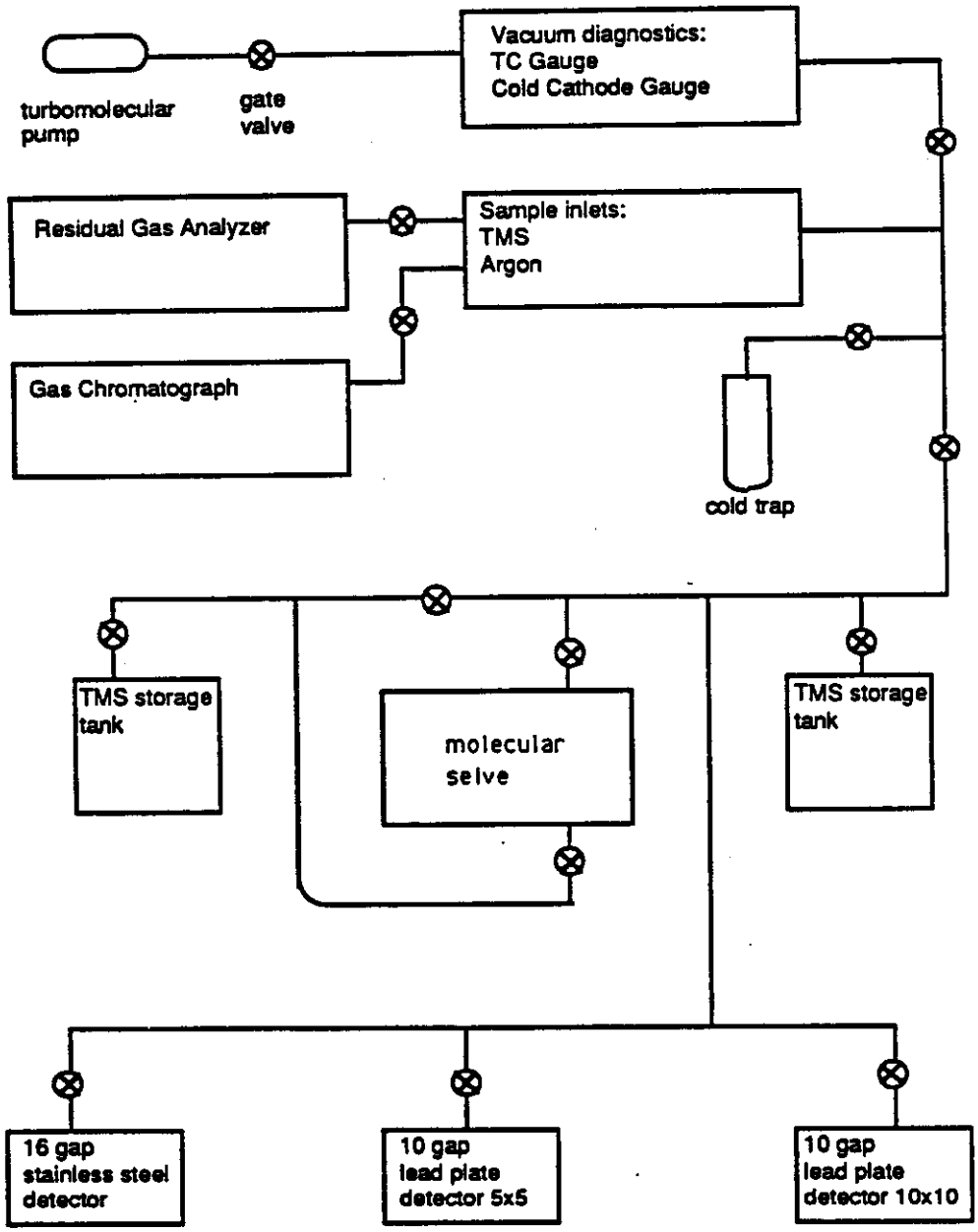

Figure 1: Vacuum layout for the PENN TMS system

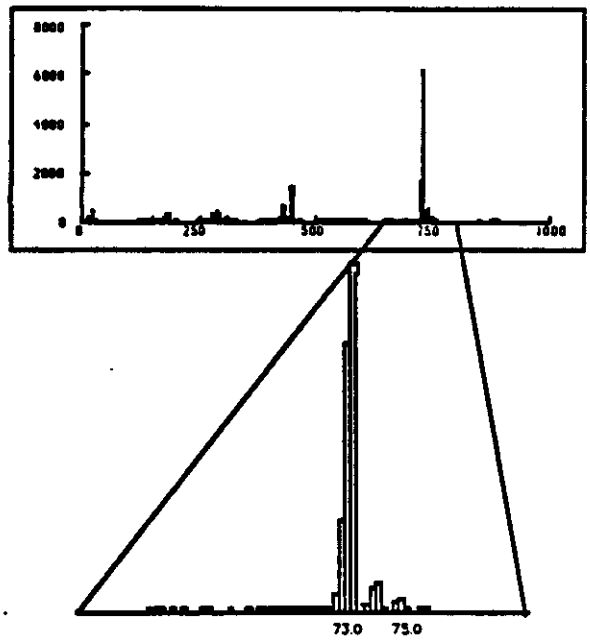

Figure 2: TMS sample Mass Spectrometer signal.

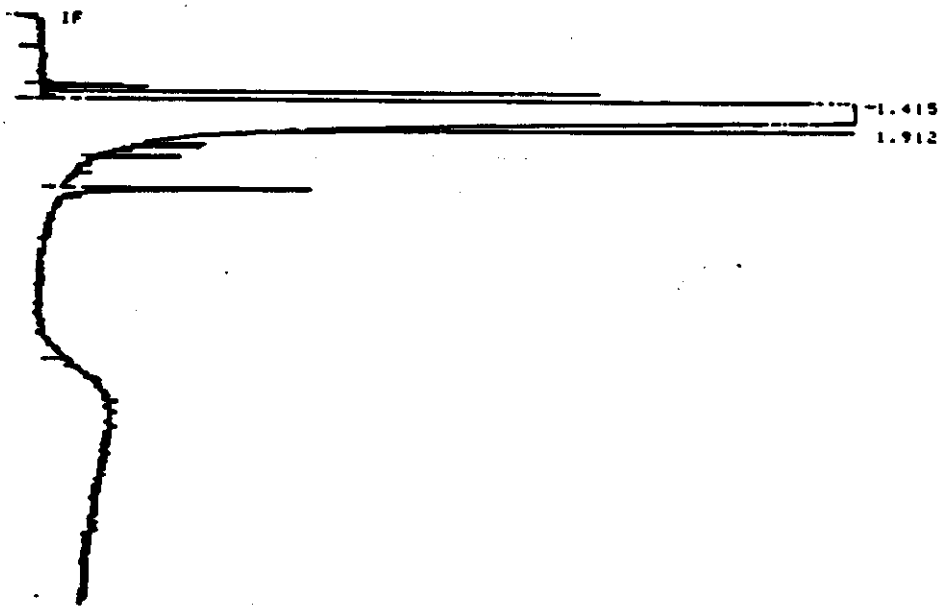

Figure 3: TMS sample Gas Chromatograph trace.

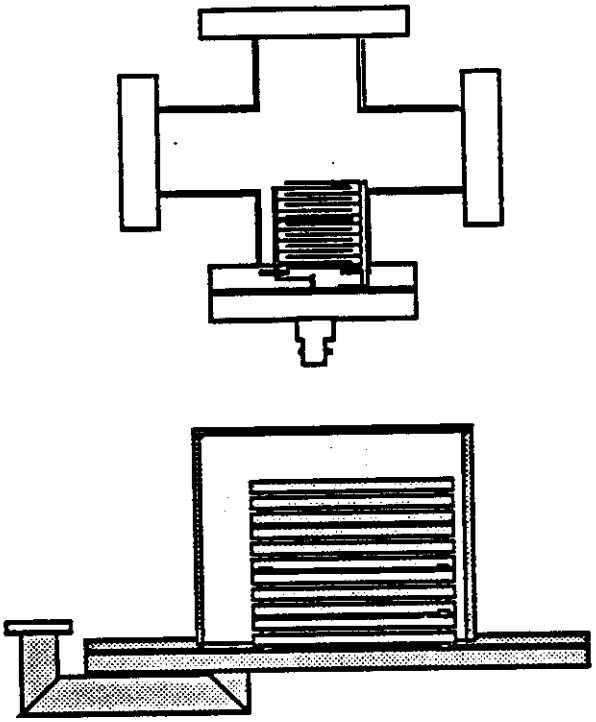

Figure 4: 16 gap stainless and the 10x10cm lead plate detectors.

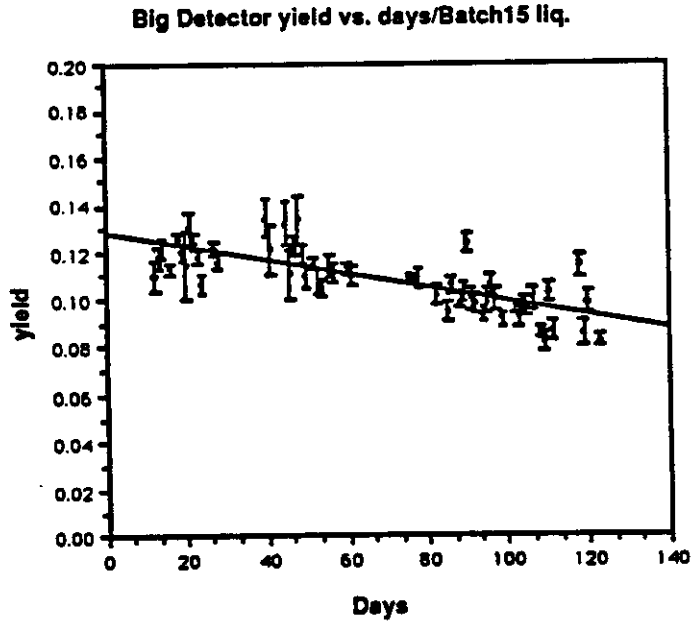

Figure 5: Time dependence of the yield from the big detector with TMS in direct contact with the lead plates.

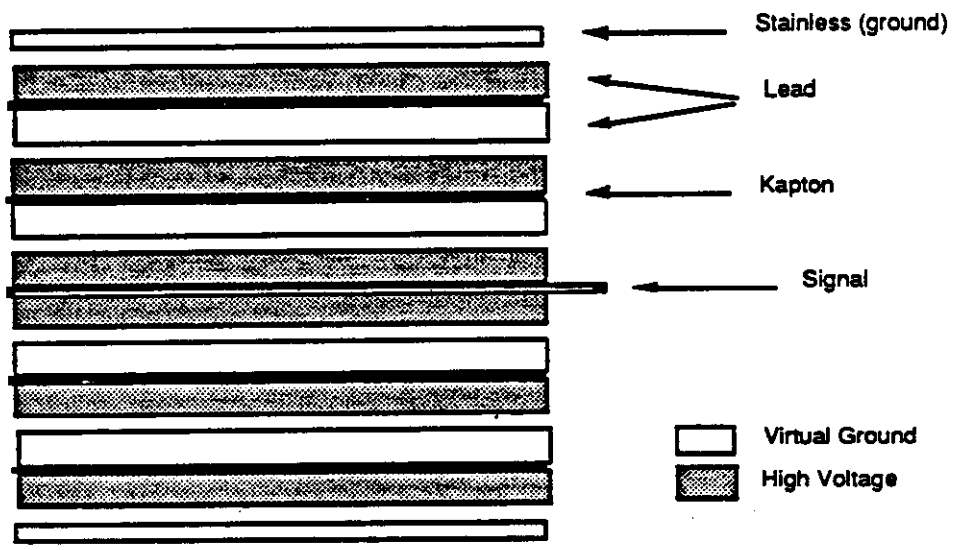

Figure 6: Single stack(1x1) prototype using all of the TBM construction techniques.

module has 6 gaps of 2mm each with single kapton foils between pairs of lead plates, and is connected in the form of an electrostatic transformer (see figure 6.)

Tests performed during the past year include:

1. Continued studies of the yield versus voltage curve for samples in the stainless detector. Comparisons are made between the shape of this curve and the Onsager theory to extract electron lifetime and charge recombination radius (see figure 7). Measurements at high voltage are used to compare the electron yield achieved from different batches of the liquid each with slight modifications to the purification procedure.

2. Measurements of the yield in the small lead detector and studies of the relative calibration of the amplifier systems on the lead and stainless detectors.

3. Yield measurements on the big lead detector as a function of time until a degradation could be measured. The results of these measurements were shown previously in figure 5. The measured degradation looks small enough that a modest amount of cleaning of the liquid should be sufficient to keep a detector functioning for years. Studies continue to try to find the origin of the effect. There are at least three possibilities. The detector is sealed with a 20cm diameter Viton ring which has a potential leak rate sufficient to explain the effect. Future modules will incorporate a standard copper gasket and conflat flange to eliminate this possibility. It is also possible that the contaminant is leaching slowly from the lead plates, or, the contamination may be the result of water and oxygen desorption from the stainless steel module walls. For the latter case, consultation with the surface experts in the condensed matter group at PENN has indicated that it may be useful to design the vacuum walls from Aluminum instead of stainless. While more difficult to weld, the Aluminum provides much better vacuum desorption properties than the stainless. This is fortunate since in the EG&G design for a full size SSC calorimeter in which we participated, it was found that replacing some

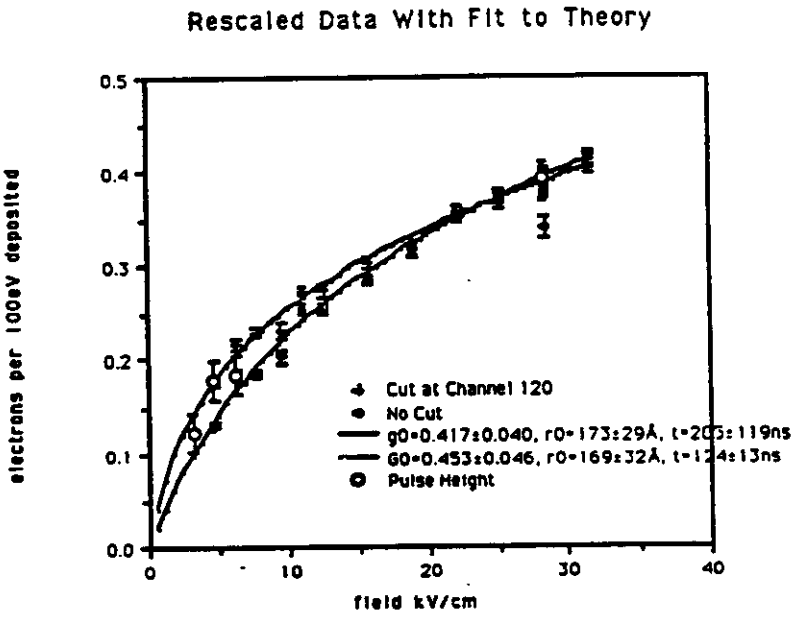

Figure 7: Comparison of the yield vs HV for Onsager theory.

of the structural materials with Aluminum was desirable from the standpoint of minimizing the amount of dead material seen by particles interacting in the calorimeter.

4. Comparisons were made between several preamps and post amplifiers in order to minimize the noise. This is particularly important in the case of the full scale lead detector which has an input capacitance of almost 1 nf. This large input capacitance makes it difficult to design low noise high speed electronics for the calorimeter front end. The best performance to date has been achieved using a Rel-Labs preamp with standard spectroscopy amplifiers.

5. During the past year we installed the mass spectrometer system and have been using it to collect spectra of the TMS samples as they come from the vendor and after they have been purified. Work is underway on software to extract peaks from these spectra and to use the splitting patterns and isotopic abundance tables to identify contaminants.

6. A gas chromatograph was attached to the system with a standard detector and a detector which is specifically sensitive to compounds which will affect electron lifetime in the liquid.

7. The electronics has been modified to allow the digitization of the pulses using a Lecroy waveform digitizer. Individual pulses are then sent to the computer (which is a MacIIC using a Micron interface and the MacSys software from CERN) which then stores the data and performs pulse averaging. Pulses are fit to extract the lifetime of the electrons in the liquid. An example of the pulse shape and fit is shown in figure 8. The electronics response function must be known in order to extract the electron lifetime from this type of data. This is done by running the detector at high voltage. At 4500V for example, the drift time in our detector is 58ns which represents almost an impulse input for the amplifiers. Electronics rise and fall times are adjusted to fit the high voltage data (see figure 9).

8. Modifications of the basic purification procedure have been tried including multiple passes through the molecular sieve, high speed versus slow speed transfers, and low temperature

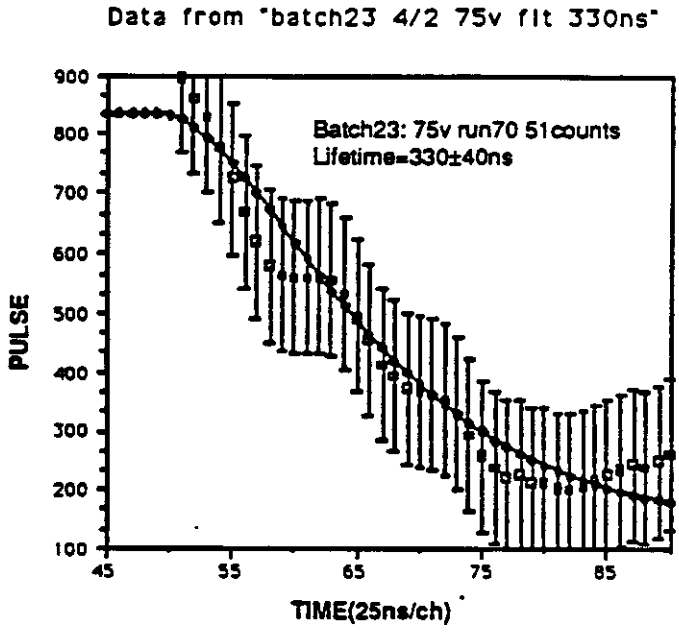

Figure 8: Average pulse waveform with a fit for the electron lifetime.

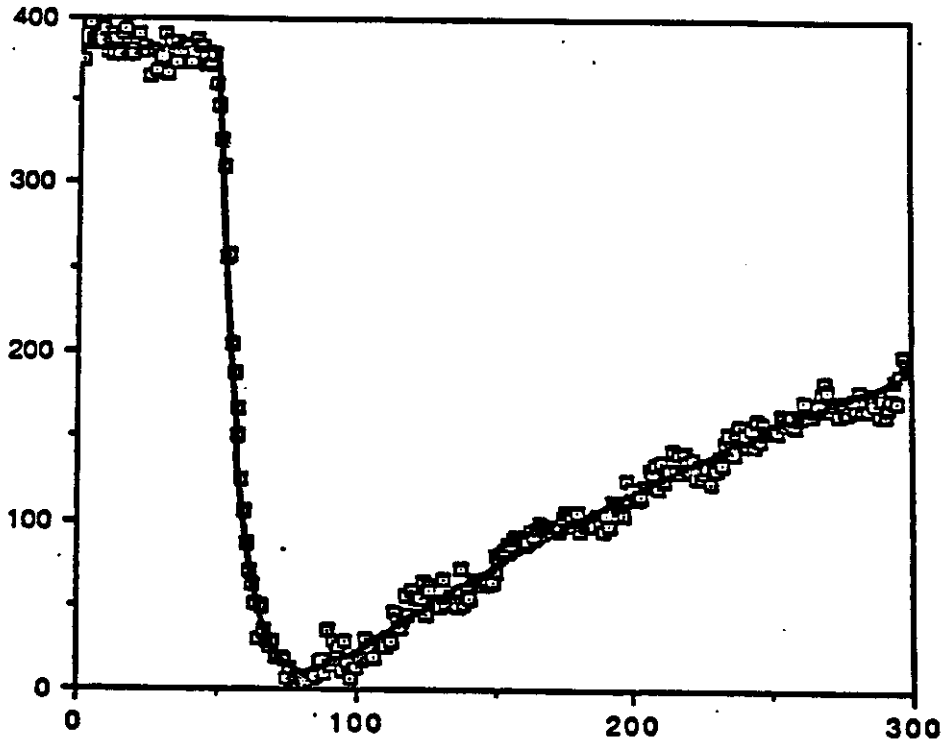

Figure 9: Average pulse waveform at high voltage with a fit for the electronics response.

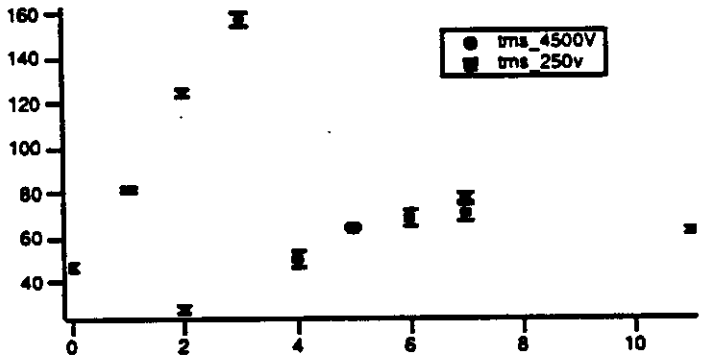

Figure 10: Pulse height in the 10 gap lead detector as a function of the number of cleaning cycles.

versus high temperature distillation.

9. An electronics configuration for the TBM has been developed using a slightly modified version of the BNL electronics for liquid Argon tests.

10. The two liquid samples which had been in contact with lead for 9 months were removed from the detectors. The first sample was analyzed using the mass spectrometer and showed significant extra peaks corresponding to water, carbon monoxide and carbon dioxide. The water peak was probably due outgassing from the lead plates, but might also be due to the poorer purification procedures in use at the time these liquid batches were produced. The second batch of liquid was repurified and put back into the detector to demonstrate that the contaminants could be removed using a molecular sieve.

11. Cyclic purification of small amounts of liquid was tried with good results. We are also investigating the use of pumps for circulating small quantities of the liquid. These pumps are normally used for high purity water and other chemical transport. Figure 10 shows the pulse height obtained as a function of the number of purification cycles. After 2 cycles, the voltage on the stack was lowered to provide more sensitivity to contaminants. Figure 11 shows a comparison of the mass spectra for two sequential cycles. The differences are small except in the region below 5 and around the water peak at 18.

12. Initial pumpdown tests were conducted on the 1x1 module (see figure 12.) The mass spectrometer was used to monitor the outgassing products. The major souce was water, probably from the lead and kapton surfaces. Because of the small spaces between the lead and kapton, it was feared that the module could be quite difficult to pump. This was not the case.

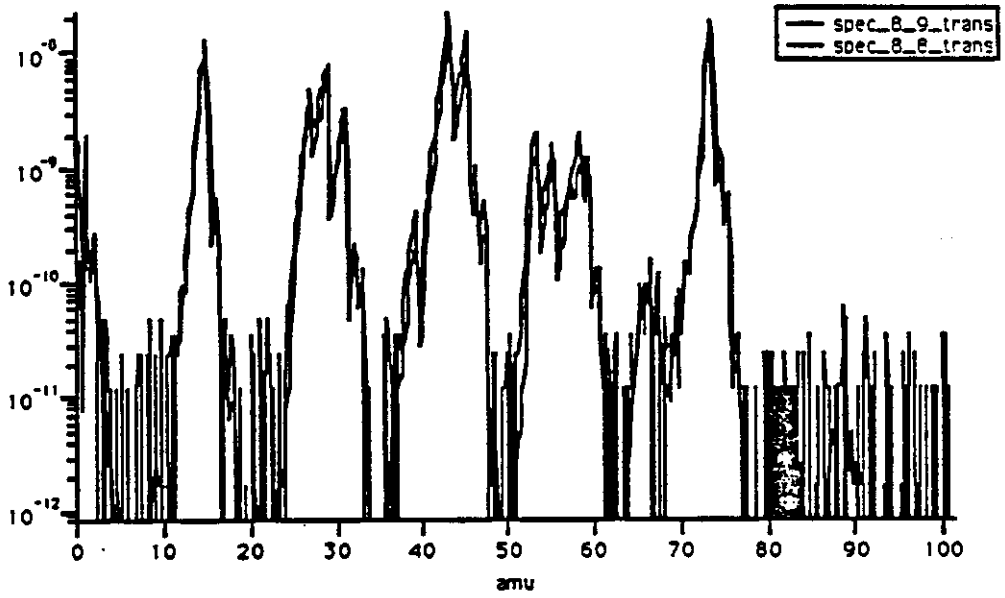

Figure 11: Comparison of the mass spectra for two sequential cleaning cycles.

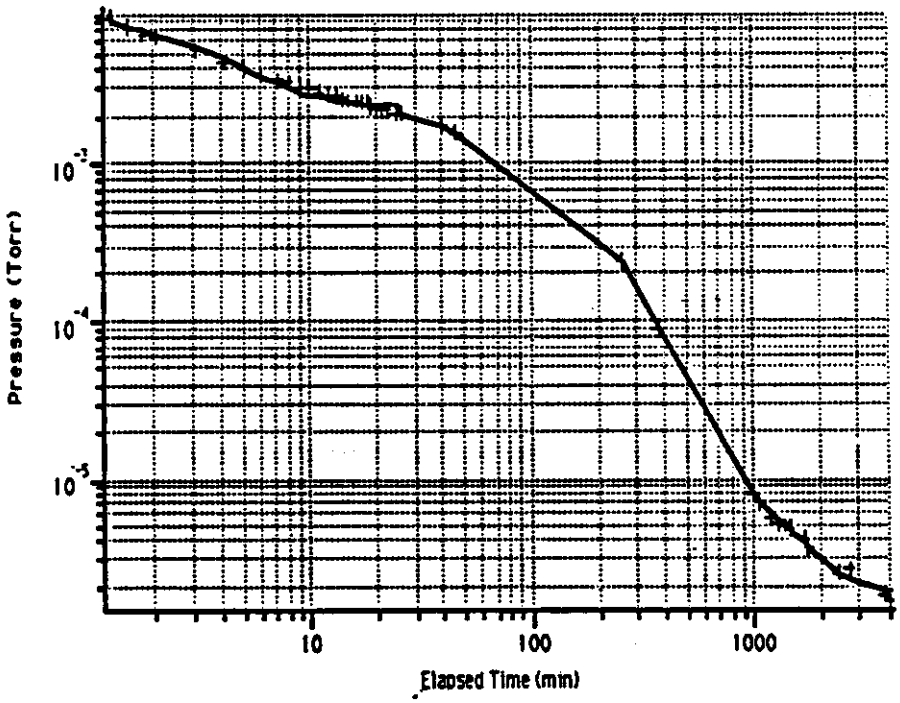

Figure 12: Pumpdown curve for the 1x1 module. Outgassing products were water, carbon monoxide and carbon dioxide.

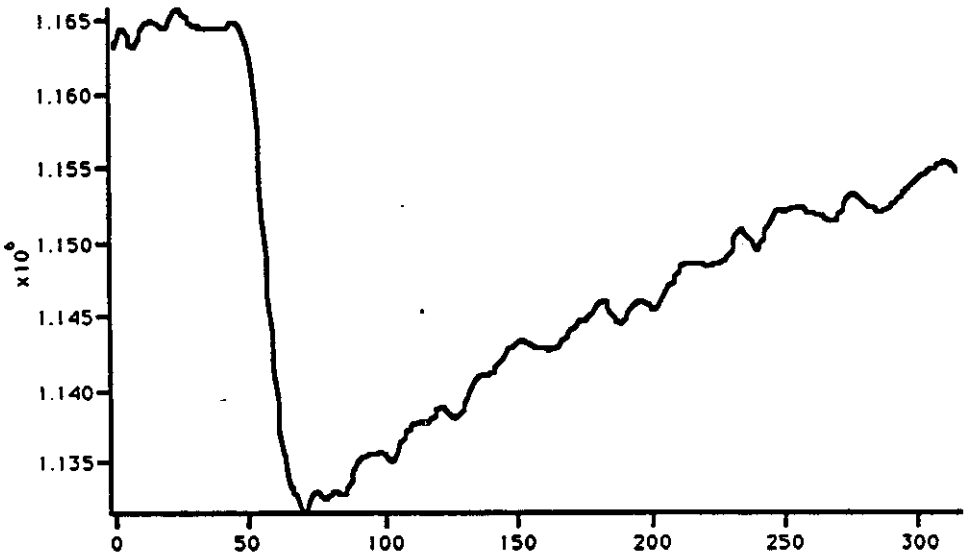

Figure 13: Pulse average shape from the electrostatic readout chamber (1x1).

Plans for Next Year

The program for the next year will include

1. Continued optimization of the purification procedures for TMS
2. Installation of leak valve system so the mass spectrometer can be used during high pressure liquid transfers
3. Calibration of gas spectrometer columns and detectors and use of chemical search libraries to identify the six unknowns found in TMS
4. Testing of the 1x1 module prototype of the TBM stack design and measurement of the rate at which TMS is poisoned by the materials in the TBM. Figure 13 shows the pulse shape of signals observed in the chamber.
5. Replacement of the stack glass resistors with carbon resistors in the 1x1 stack
6. Installation and filling of a 2x1 stack prototype being constructed at Berkeley
7. Use of Argon and Nitrogen gases and liquid pumps to replace cryopumping and pouring techniques for liquid transfer.
8. Testing and installation of TBM electronics based on the BNL liquid Argon system.
9. System engineering issues for the large subsystem including integration of barrel, plug, and forward calorimetry and implications of coil geometry for electromagnetic calorimetry performance.

Simple methods are now available for the purification of TMS, and the operation of this liquid in the presence of lead calorimeter plates brings us much closer to being able to design TMS detectors using well-proven liquid Argon technology. A great deal of progress has thus been made in the last two years in the study of room temperature liquids for ionization calorimetry, and this new technology continues to be an interesting candidate for future calorimeter designs requiring fast, compensating and radiation hard sampling media.

United States Department of Energy
University of Pennsylvania

EXPLANATION of BUDGET ITEMS

Super Conducting Supercollider: Large Subsystem Warm Liquid Purity

A-II(a) REIMBURSEABLE or COST-SHARING PORTION

1. Salaries & Wages
2. Employee Benefits

EMPLOYEE	RANK	MAN MONTHS	SALARY	BENEFITS	TOTAL
Katz, C.	Technician	12	20,350		
Gregory, M.	Undergraduate	6	8,500		
Newcomer, F.M.	Elect. Engineer	1	4,165		
Certok	Graduate	12	12,907		
			45,924	8,255	54,179

3. Domestic Travel
One one week trip from Philadelphia, PA. to Dallas, Tx.
$550 for airfare, $250 for subsistence 800

4. Indirect Costs @ DHHS Approved rate of 65% of MTDC 35,736

5. Tuition 6,390

6. EQUIPMENT 96,000

a.	Gas Chromotography/ Mass Spec PC & Library	15,000
b.	Vacuum Components	35,000
c.	TMS/TMP (liquids)	7,000
d.	Test Modules	20,000
e.	CAMAC/FASTBUS/DAQ for TBM	15,000
f.	Power Supplies	4,000

TOTAL SSC SUBSYSTEM FUNDS REQUESTED: 193,105

It is requested that the Department of Energy provide 100%
of the A-II(a) portion of $165,000
The University of Pennsylvania hereby certifies that equipment
requested is not available within our institution.

The University of Alabama

Department of Physics and Astonomy

Tuscaloosa, Alabama 35487-0324

Summary

We report the first year progress on a Subsystem R&D program to develop fast, radiation-hard calorimetry for the SSC. This work is a continuation and expansion of research previously supported by the generic detector R&D program to develop fast warm liquid calorimetry for the SSC. A unique and distinguishing feature of the research proposed here is the speed with which this calorimeter can respond, compared to other liquid ionization techniques. This technique has general applicability for any experiment needing radiation-hard instrumentation, particularly in the forward region, with a response time matched to the SSC beam crossing. Radiation damage tests are presently underway to determine the detector's response and optimization to conditions expected in the forward region.

August 1990

Fast Measurement Electronics for Warm Liquid Calorimetry

With the development of fast, radiation-hard charge amplifiers for warm liquid calorimetry [1], fast detector response is possible despite the relatively slow drift velocities in these liquids. In response to the repetition rate of the SSC (16 nsec) only the very front spike of the ionization signal will be used. Under these conditions only moderately severe purity requirements need be met: Free electron lifetimes of ≥ 1 μsec are more than sufficient for adequate charge collection efficiency.

To maintain the intrinsically fast response of the of the front-end electronics (less than 10 nsec), the preamplifier must be mounted directly on the detector. Detector capacitance, in turn, must be kept as low as possible. For a pad size of 20 × 20 mm^2 and dual 2.5 mm gap suitable for a fast calorimeter design, the corresponding source capacitance (5.4 pF) will easily guarantee an amplifier risetime between 5 nsec and 10 nsec on the basis of previous design considerations for fast, front-end electronics [2]. (See Appendix for earlier test results.)

Signal/Noise Considerations

The maximum current signal within a liquid ionization detector cell is [3]:

$$I(t) = N \cdot e \cdot \frac{v}{t_d}(1 - \frac{t}{t_d}),$$

where N is the total number of free electron-ion pairs produced in the ionization gap of length d moving with velocity v during a maximum drift time t_d. The corresponding amount of charge produced in the cell is then:

$$Q(t) = N \cdot e \cdot \left[\frac{t}{t_d} - \frac{1}{2}(\frac{t}{t_d})^2\right] - \frac{N \cdot e}{2}$$

For the dual 2.5 mm gap proposed for this detector, approximately 10,000 free electrons are produced in TMS per minimum ionizing particle, yielding a maximum total charge of some 5,000 electrons within 1 nsec of charge particle traversal. At an applied operating voltage of 12.5 kV, the maximum free electron drift time within the detector is 50 nsec. This field value (50 kV/cm) is determined by

practical experience with high voltage breakdown due to dust particle contamination within the liquid [4].

A significant reduction in the total number of detector readout channels can be achieved by connecting individual gaps in parallel along a longitudinally projective tower axis within one supermodule. In this way, the total charge signal collected by one preamplifier is proportional to the total number of cells connected, while the optimized preamplifier noise increases only in proportion to the square root of the number of cells [5]. The resulting signal-to-noise ratio for this configuration is then increased by the square root of the number of gaps connected in parallel:

$$\left(\frac{Signal}{Noise}\right)_{M\ gaps} = \sqrt{M}\left(\frac{Signal}{Noise}\right)_{single\ gap}$$

The maximum number of gaps one can connect in parallel is ultimately determined by the risetime and shaping requirements of the front-end charge preamplifier, described below.

Charge Preamplifier Design

The charge preamplifier schematic for the proposed warm liquid calorimeter is shown in Figure 1. This circuit has been especially designed to compensate for parameter changes due to high radiation exposure which include the loss in transistor β [6]. SPICE simulations of this circuit have been performed using the latest (dot-model) parameters for polysilicon BiFET technology presently available from Harris Semiconductor Corporation, both for pre-radiated and post-radiated conditions. This industrial BiFET process has a measured radiation hardness of 4×10^{14} neutrons/cm^2 and nearly 50 Mrads of ionizing radiation hardness. Prototype circuits have recently been submitted to Harris Semiconductor for monolithic implementation in this technology. The estimated cost per channel from Harris is between \$0.54 and \$0.95, depending on the quantity.

The charge profile within the detector cell was modeled according to the prescription in reference [3] and is plotted in Figure 2 for a source capacitance

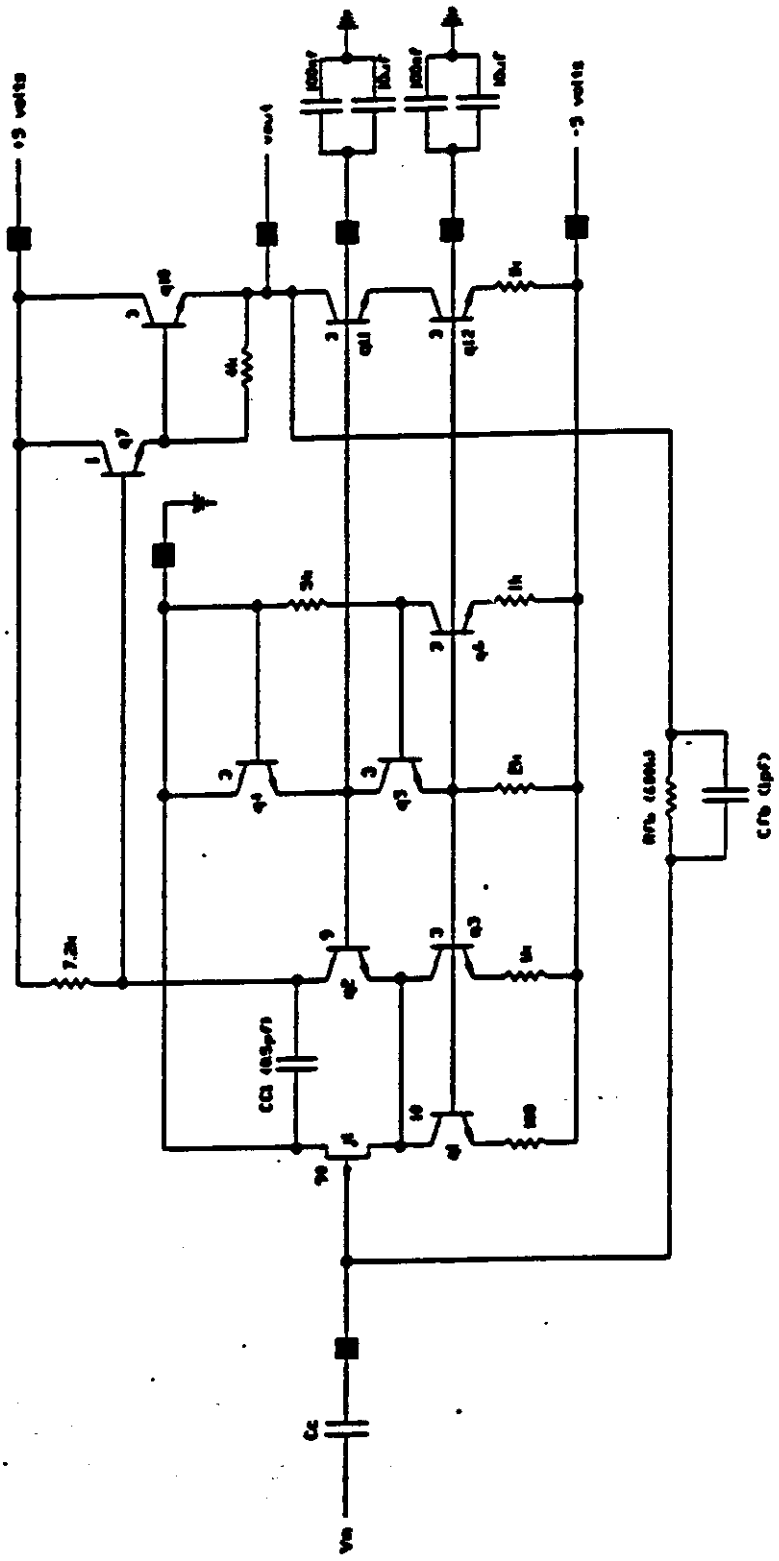

Figure 1. Charge preamplifier circuit schematic.

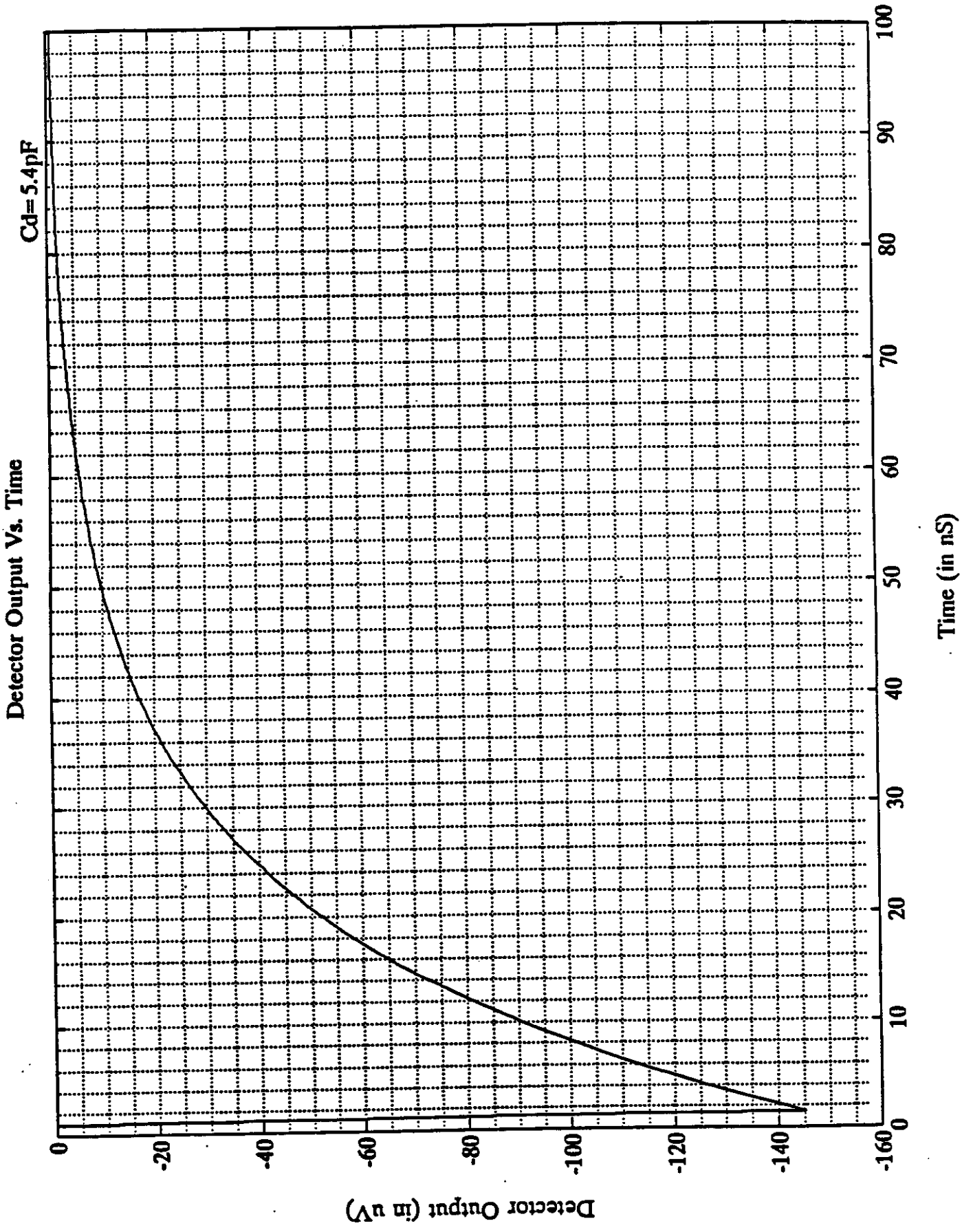

Figure 2. Time dependence of input charge signal, C_d = 5.4 pF, t_d = 50 nsec.

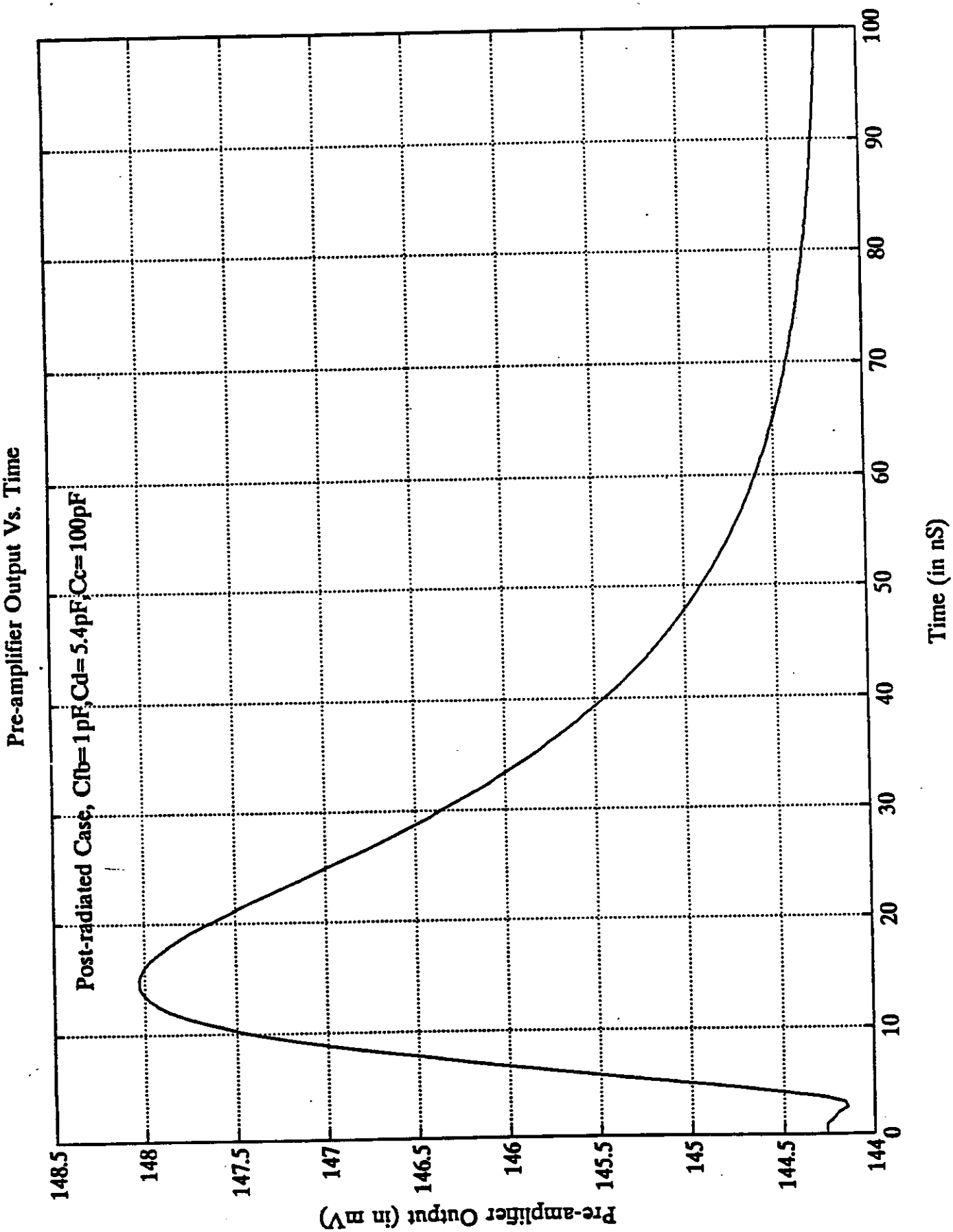

Figure 3. Preamplifier output response to detector input of Figure 2.

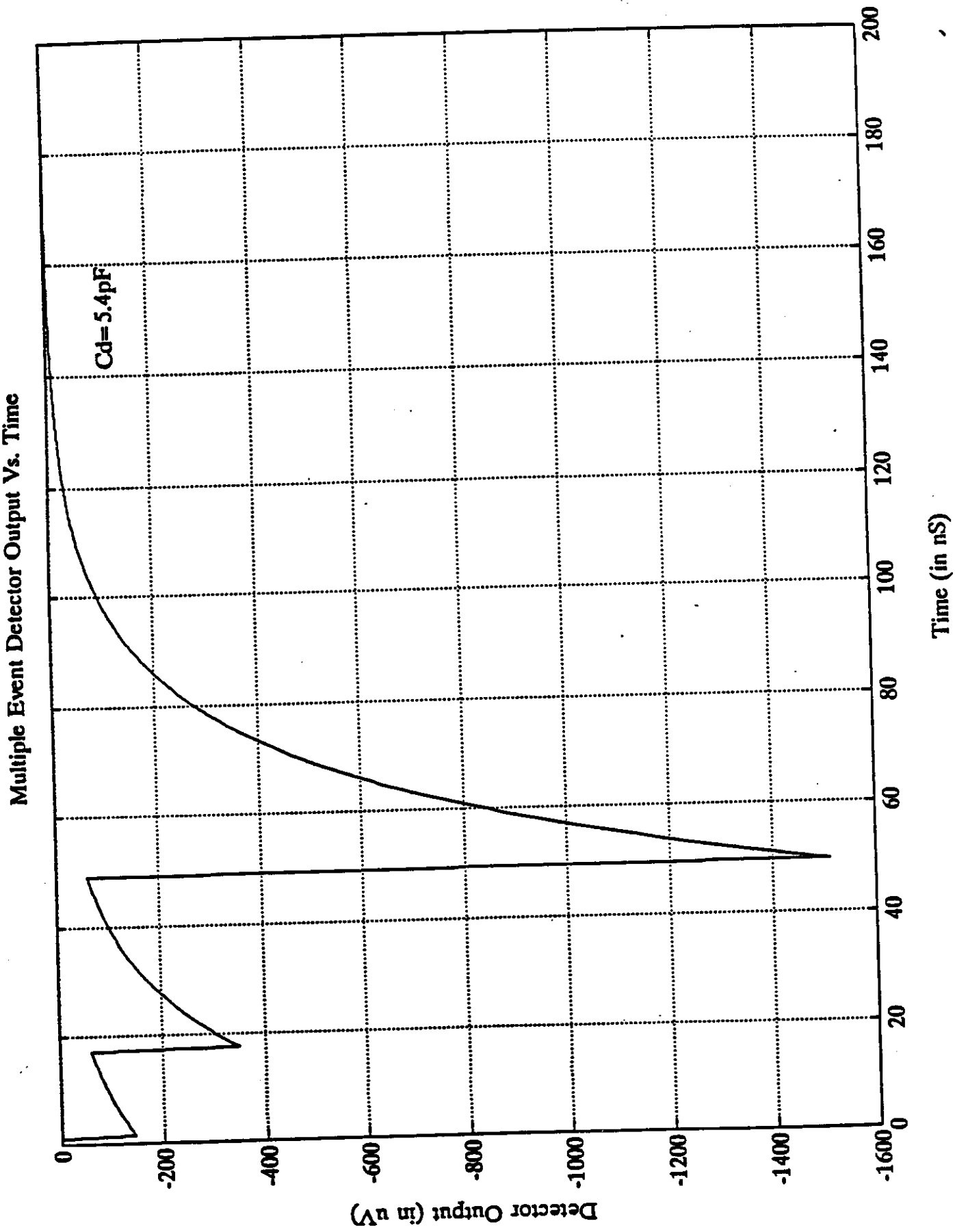

Figure 4. Detector output: (1,2,10) particles in 4 consecutive crossings, C_D = 5.4 pF.

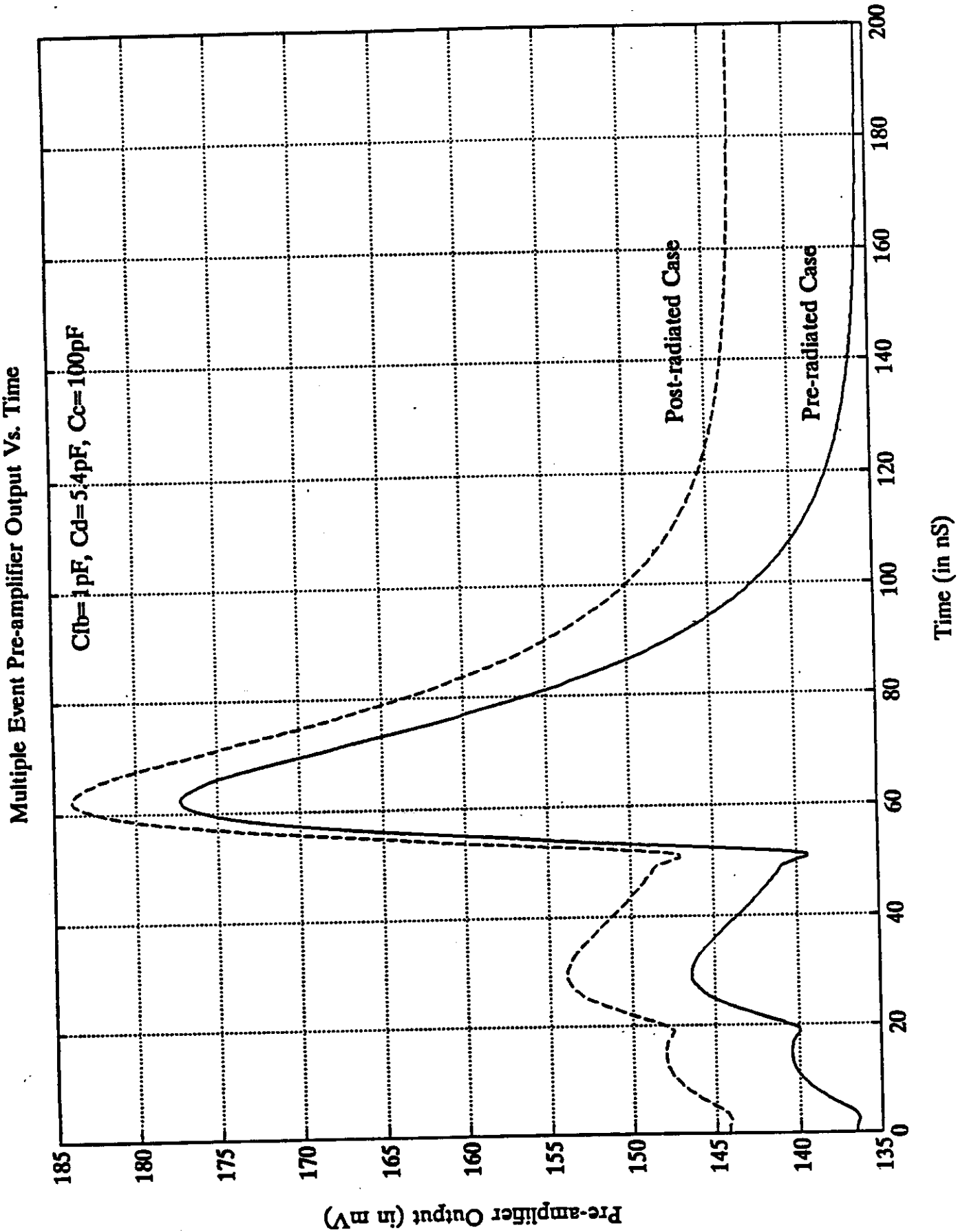

Figure 5. Preamplifier output response to detector input of Figure 4.

of 5.4 pF. The maximum drift time in this cell is only 50 nsec. The resulting preamplifier output is shown in Figure 3 for this charge input. Note that for a minimum ionizing particle, this amplifier responds with a gain of approximately 5 V/pC (ΔV = 4 mV) and a risetime and sampling time that is well within the 16 nsec bunch spacing. The corresponding settling time of the amplifier is also seen to lie within the maximum (50 nsec) drift time. The baseline (dc) voltage of 144 mV is required to bias this circuit. The remaining voltage range available from this baseline allows for at least 1200 minimum ionizing tracks to be detected within a 16 nsec sampling time, without saturating the amplifier. In Figures 4 and 5 we show the detector and preamplifier response, respectively, to 1, 2, and 10 particle traversals occuring in 4 consecutive 16 nsec SSC beam crossings. These plots show the feasibility of the proposed design to resolve complex events with a bandwidth matched to the SSC repetition rate.

The signal-to-noise ratios for this circuit is calculated in Tables 1-7 for detector capacitances of 5.4, 10, and 100 pF and for various decoupling capacitances. For the minimal 5.4 pF source capacitance, the expected signal-to-noise ratio is approximately 5:1. Note that this ratio decreases for higher source capacitance, assuming only one charged particle traversing the gap. However, when multiple gaps of smaller capacitance are connected in parallel, the corresponding signal is then multipled by the additional number of gaps (compare values for C_d = 10, 100 pF). Note also that for 100 pF source capacitance, the rms noise decreases with increased decoupling capacitance. An additional factor of $\sqrt{10}$ in the signal-to-noise ratio can be attained for even higher values of C_e. However, the risetime and shaping time of the amplifier then exceed then 16 nsec sampling period.

Digitizing and Buffer Circuits

Experience with the L3 hadron calorimeter at CERN [7] suggests that a 16 bit ADC will be necessary to achieve a 0.5% absolute energy calibration of the proposed warm liquid calorimeter. The single bit resolution for this configuration is then 100 μV, which is matched to the input referred noise of 890 electrons

(rms) for a 5.4 pF source capacitance, $(\Delta V_{rms})_{output} = 130\ \mu V$. The 16 nsec ADC design is based on a serial-parallel folded architecture and is described elsewhere in more detail [8]. In this scheme the conversion takes place during two time periods. In the first period, a rough quantization is performed by an eight-bit ADC and a digital-to-analog converter (DAC) settles to a final output value. In the second period, the quantized signal is subtracted from the sampled analog input signal and is applied to a second eight-bit ADC for fine quantization to a digital signal. This converter results in conversion performance similar to that of flash techniques [9, 10] with circuit complexity and power dissipation that are significantly reduced. Only 24 comparators are required compared to the 255 comparators normally used in an eight-bit flash converter.

A buffer memory immediately after the ADC is proposed with enough memory to store one μsec of data for first level triggering. The data buffer and all electronics that follow will be located on the outer surface of the calorimeter system, outside the high radiation area. Accordingly, we propose to fabricate the data buffer in a high-radiation CMOS technology to take advantage of circuit density and low power requirements of CMOS technology. Up to eight ADC/memory channels and read/write circuits are planned per chip.

References

1. D. DiBitonto et al., "Fast, Radiation-Hard Charge Preamplifiers for Warm Liquid Calorimetry," Proceedings of the Workshop on Calorimetry for the Supercollider, March 13-17, 1989, Tuscaloosa, AL, p. 583 (World Scientific publ.).

2. D. DiBitonto et al, "Advanced Forward Calorimetry for the SSC and TeVatron Collider," NIM A279 (1989), 100.

3. W.J. Willis and V. Radeka, "Liquid-Argon Ionization Chambers as Total-Absorption Detectors," NIM 120 (1974), 221.

4. R.C. Muñoz, J.B. Cummings, and R.A. Holroyd, "Ionization of liquid hydrocarbons and tetramethylsilane by ^{241}Am alpha particles," J. Chem Phys. 85 (2) (1986), 1104.

5. V. Radeka and S. Rescia, "Speed and Noise Limits in Ionization Chamber Calorimeter," NIM A225 (1988), 228.

6. L. Wurtz and D. DiBitonto, "Design of a High-Performance, Charge Preamplifier for the Superconducting Super Collider," to be published in IEEE Transactions on Nuclear Science.

7. L3 Collaboration, B. Adeva et al., "The Construction of the L3 Experiment," NIM A289 (1990), 35.

8. "R&D Proposal for a Fast, Radiation Hard Calorimeter Subsystem for the SSC," submitted to the SSC Laboratory (October 1989).

9. R. Van de Plassche and P. Baltus, "An 8b, 100 MHz A/D Converter with 500 MHz Resolution Bandwidth," ISSCC Dig. of Tech Papers, Feb. 1988.

10. Y. Yoshi et al., "8b 350 MHz flash ADC," ISSCC Dig. of Tech Papers, Feb. 1987.

Table 1: Charge pre-amplifier performance with $C_d = 2.7pF$, $C_{Fb} = 1pF$

C_c (pF)	τ_r (nS)	S_p (nS)	Gain (V/pC)	Input inferred noise (e^- RMS)	S/N
10	5.5 (5.5)	10.5 (10.5)	1.5674 (1.6047)	1888 (1829)	2.6480 (2.7340)
50	6.0 (5.5)	12.5 (12.5)	6.0659 (6.2171)	600 (582)	8.3330 (8.5910)
100	6.5 (6.5)	13.5 (13.5)	9.4242 (9.6864)	445 (431)	11.2360 (11.6010)

Power Dissipation 45.1 mW (45.6 mW)

- ( ) ← Pre-radiated data, all other data post-radiated.
- C_d ← Detector capacitance.
- C_c ← Coupling Capacitance.

Table 2: Charge pre-amplifier performance with $C_d = 5.4pF$, $C_{Fb} = 1pF$

C_c (pF)	τ_r (nS)	S_p (nS)	Gain (V/pC)	Input inferred noise (e^- RMS)	S/N
10	5.5 (5.0)	10.5 (10.5)	0.7837 (0.8021)	3780 (3660)	1.3228 (1.3661)
50	6.0 (6.0)	12.5 (12.5)	3.0298 (3.1080)	1202 (1163)	4.1597 (4.2992)
100	7.0 (7.0)	13.5 (13.5)	4.7104 (4.8433)	890 (862)	5.6180 (5.8005)

Power Dissipation 45.1 mW (45.6 mW)

Table 3: Charge pre-amplifier performance with C_d = 10pF , C_{Fb}=1pF

C_e (pF)	τ_r (nS)	S_p (nS)	Gain (V/pC)	Input inferred noise (e^- RMS)	S/N
10	5.0 (5.0)	10.5 (10.0)	0.4282 (0.4338)	6689 (6910)	0.7475 (0.7236)
50	6.5 (6.5)	12.0 (12.0)	1.6544 (1.6826)	2200 (2136)	2.2727 (2.3408)
100	7.5 (7.5)	13.0 (13.0)	2.5674 (2.6408)	1633 (1581)	3.0618 (3.1626)

Power Dissipation 45.1 mW (45.6 mW)

Table 4: Charge pre-amplifier performance with C_d = 100pF , C_{Fb} = 1pF

C_e (pF)	τ_r (nS)	S_p (nS)	Gain (V/pC)	Input inferred noise (e^- RMS)	S/N
10	5.5 (5.5)	10.5 (10.5)	0.0409 (0.0433)	72K (68K)	0.0694 (0.0735)
50	6.5 (6.5)	12.0 (12.0)	0.1645 (0.1662)	22K (22K)	0.2273 (0.2273)
100	7.5 (7.5)	13.5 (13.5)	0.2562 (0.2639)	16K (16K)	0.3125 (0.3125)
200	8.0 (8.0)	15.5 (15.0)	0.3516 (0.3632)	13K (13K)	0.3637 (0.3766)
500	8.5 (8.5)	16.5 (16.5)	0.4582 (0.4737)	12K (12K)	0.4105 (0.4176)

Power Dissipation 45.1 mW (45.6 mW)

CHARGE TRANSFER and SIGNAL GANGING

Wenzel, 1/19/90
GIN-314, IEEE, S.F.

Compare FCT and EST for NC = 10 nF, $\tau = R_a C_S = 25$ ns

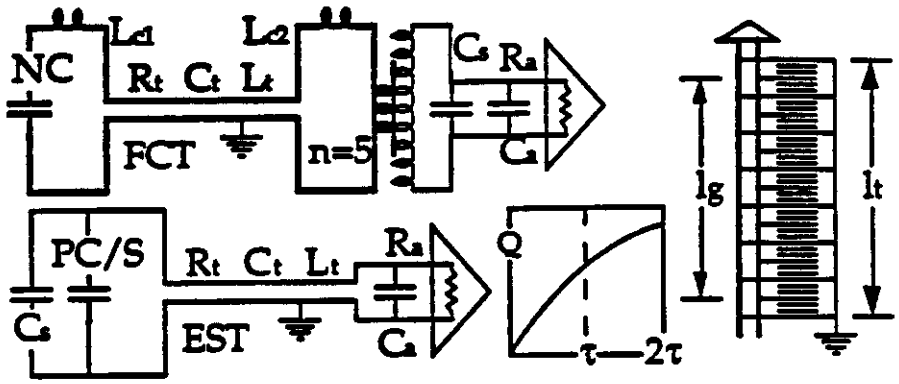

C_S = 10 nF (0.4 nF) for S = 1 (5)
R_a (ohms) = τ/C_S = 2.5 (62.5)
L_{crit} (nHy) = $\tau^2/4C_S$ = 16 (391)
IMPEDANCES ARE EASIER FOR EST!

SIGNAL GANGING

internal transmission line for uniform tower sampling
$t_{unloaded} = t_u = l_g \varepsilon^{1/2}/v$; $R_u = t_u/C_u$; $L_u = t_u^2/C_u$
where ganging length: $l_g = (1-2/P)\, l_{tower}$
If $C_u = gC_S$; then $t_g = t_u(1+1/g)^{1/2}$
Comparing FCT and EST, let l_{tower} = 50 cm, ε=3; P=50 (10);
then l_g = 48 (40) cm, and
t_u = 2.77 (2.31) ns.
If g=0.1, then g_{eff} =0.096 (0.08), and
t_g = 9.4 (8.5) ns
for S=1 (5), we have C_S = 10 (0.4) nF, giving
R_u = 2.9 (72) ohms
L_u = 8.0 (167) nHy EASIER FOR EST!

TRANSFORMER MATCHING

Wenzel
1/19/90
GIN-314
IEEE, S.F.

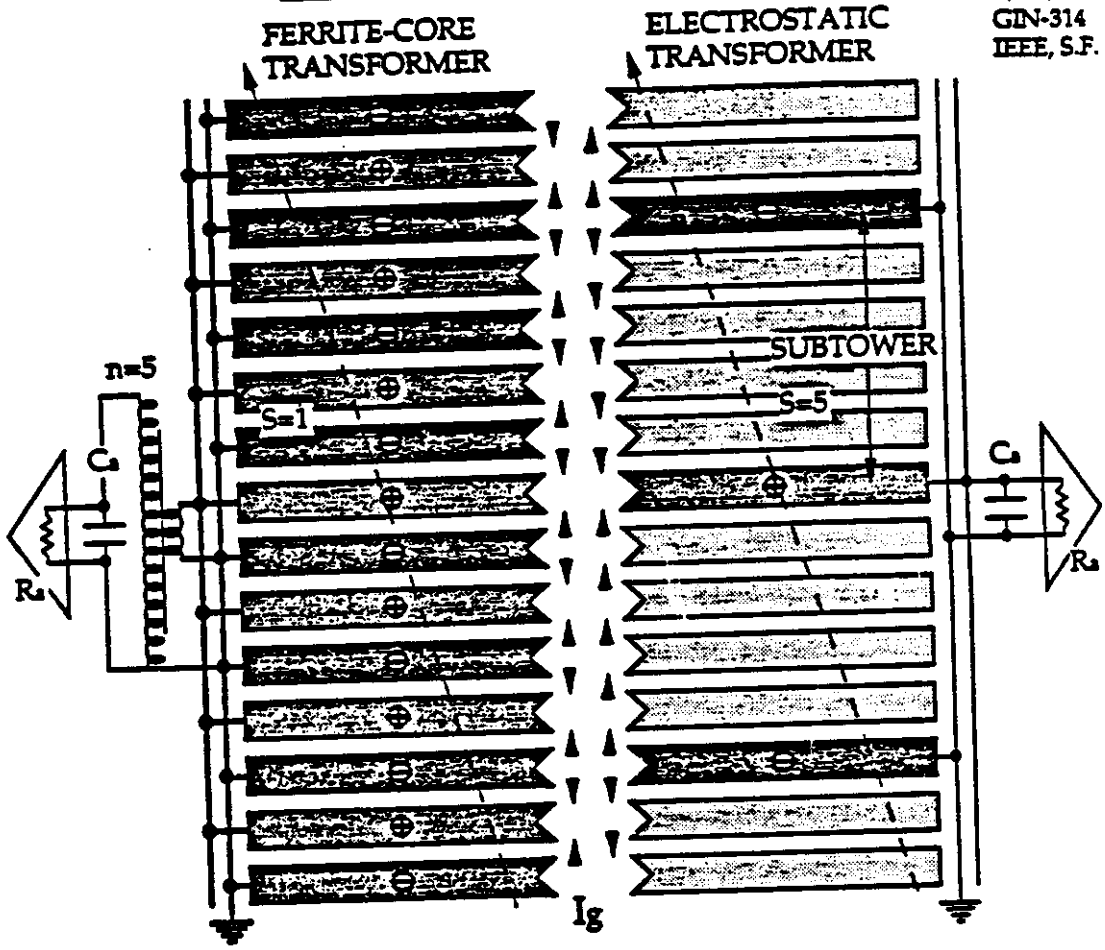

N=PS=total number of gaps in tower
P=number of parallel subtowers; S=number of gaps in series

	FCT		EST
	primary	secondary	series-parallel
transformer ratio	n		S
capacitance	NC	NC/nn	NC/SS=CP/S
signal current	ΣIg	ΣIg/n	ΣIg/S
total DC volts	V	---	SV

III. Test Results

The circuits of Figure 1 were evaluated with a 1 GHz digitizing oscilloscope (model HP54111D) and read out with an HP 9000 workstation. An HP8082A pulse generator provided a 1 nsec risetime reference. The output from this amplifier is shown in Figure 2. Tests are presently underway to evaluate the performance characteristics of this device after exposure to γ rays (order 1 Gigarad) and high neutron fluency (order $10^{14}cm^{-2}yr^{-1}$).

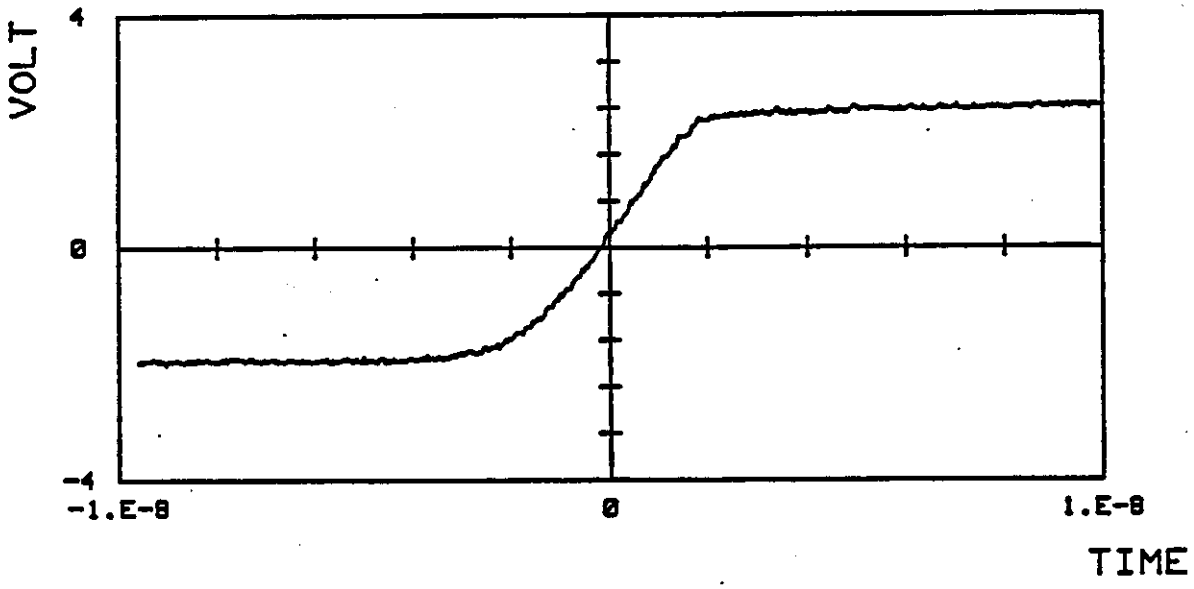

Figure 2. Output response of BiFET charge preamplifier to square wave input.

References

1. R. Wigmans, NIM A259, 389 (1987).
2. R. Holroyd, SSC-SR-1035, p. 335, June, 1988;
   R. Holroyd and D. Anderson, NIM A236, 294 (1985).
3. D. Groom, SSC-SR-1033, June 10,1988.
4. D. DiBitonto et al., NIM A279, 100 (1989).
5. D. DiBitonto et al., Proceedings of the Workshop on Calorimetry for the SSC, Tuscaloosa, Alabama, March 13-17, 1989.
6. W.J. Willis and V. Radeka, NIM 120, 221 (1974).
7. P.M. Van Peteghem et al., Proceedings of the ESSCIRC, San Francisco, September, 1989.

ELECTROSTATIC TRANSFORMERS FOR LARGE LIQUID IONIZATION CALORIMETERS[†°]

Wenzel, 1/19/90
GIN-314, IEEE, S.F.
Revised 1/90.

Lawrence Berkeley Laboratory

J. Colas*
A.B. Geyer
W.E. Hearn
M. Pripstein
G.T. Przybylski
T.F.Weber
W.A.Wenzel

[†]This work supported by Director, Office of Energy Research, Office of High Energy and Nuclear Physics, Division of High Energy Physics, of the U.S. Department of Energy under Contract No. DE-AC03-76SF00098.

° This work is part of the general program of the WALIC collaboration to study the use of room temperature liquids in SSC/LHC calorimetry.

* Permanent address: LAPP, F-74019 Annecy-le-Vieux, France.

publications and reports:

[1] J.Colas and W.A.Wenzel. "Electrostatic Transformers for Large Towers". LBL-27236. Submitted to Alabama Workshop, Tuscaloosa, 3/13-17/89.

[2] J.Colas. "Speed of Response, Pile-up and Signal to Noise Ratio in Liquid Ionization Calorimeters."Submitted to Alabama Workshop, Tuscaloosa, 3/13-17/89. Also, Submitted to ECFA Study Week, Barcelona, Spain, 9/14-21/89.

[3] J. Colas, M. Pripstein and W.A.Wenzel. "The Electrostatic Transformer". to be published in NIM.

[4] J. Colas and W.A.Wenzel. "Analytical Description of an EST". WALIC Note.

ELECTROSTATIC TRANSFORMER FOR LIQUID IONIZATION CALORIMETRY AT SSC/LHC

Wenzel
1/19/90

SSC/LHC calorimeters must be:
large, fast, hermetic and accurate in energy and position:

- ≈ 5000 tons
- >100,000 towers (electronic signal channels)
- shaping time ≤ 100ns
- $\sigma(E)/E < 5\%$ @ 100GeV.

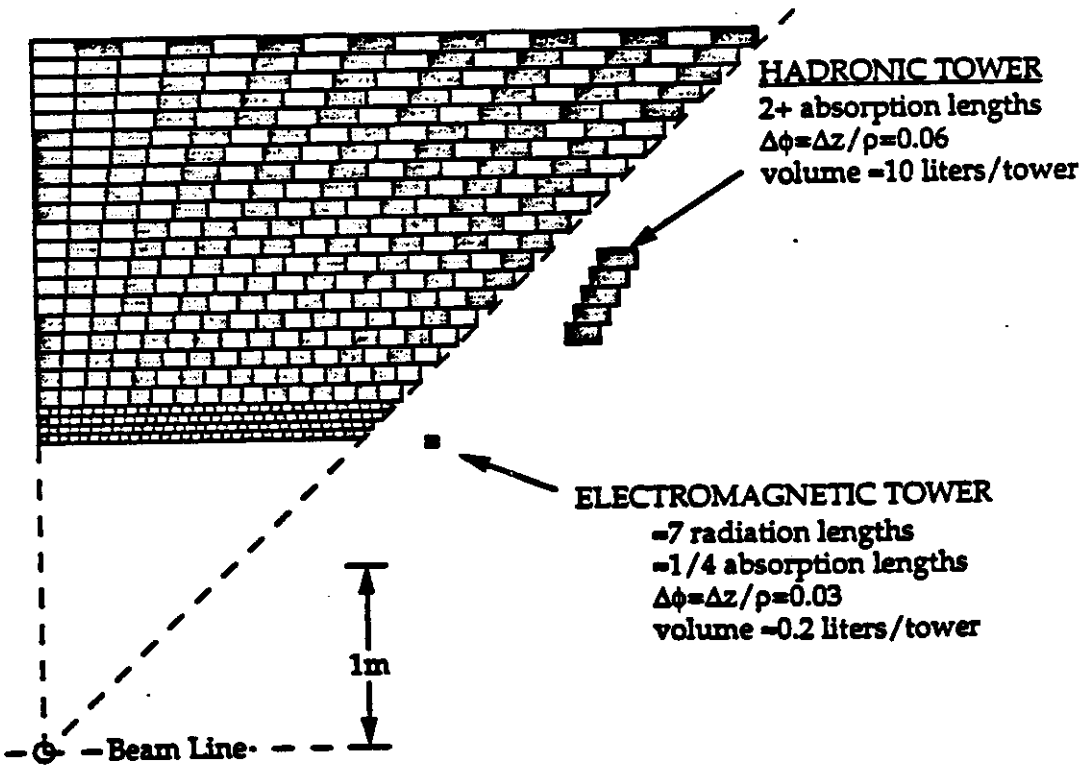

EM-HADRONIC TOWER VOLUMES DIFFER BY X50!

ELECTROMAGNETIC SECTION HAS MORE CHANNELS -
HADRONIC HAS VOLUME, MASS AND CAPACITANCE

LIQUID IONIZATION CALORIMETRY

Wenzel, 1/19/90
GIN-314, IEEE, S.F.

ADVANTAGES:
- uniformity of sampling
- gain stability
- radiation resistant
- intrinsic rise time of ionization pulse is very small

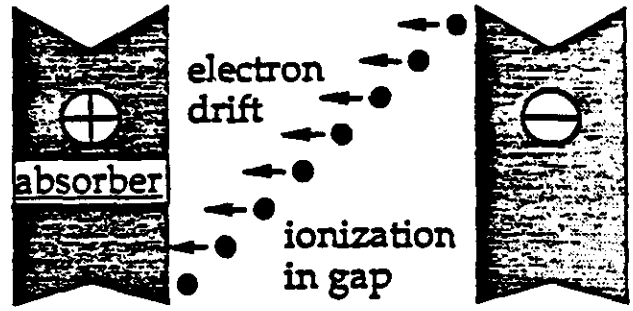

BUT:
- unit gain → small signals
- large capacitance → large charge transfer time and large noise
- background rates →measurement time <charge collection time
- For a given measurement time t_m, the useful charge is almost proportional to I_{max} and relatively insensitive to t_d.

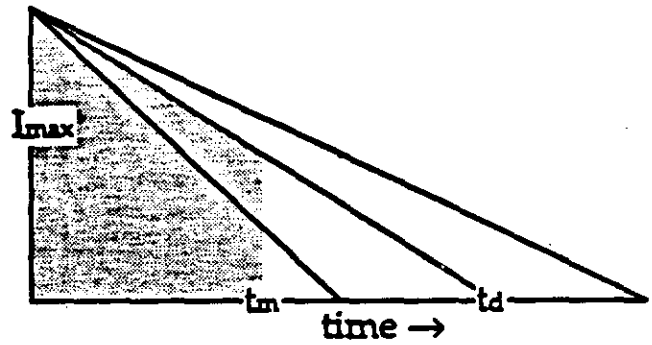

$I_{max} = (dE/dx) \times G_{fi} \times v_d$

liquid	V' kV/cm	dE/dx MeV/cm	G_{fi} ions/keV	v_d cm/μs	I_{max} ke/μs
LA	10	2.11	38	0.50	40
TMP	40	1.58	20	1.16(∝V')	37(∝V')
TMS	20	1.36	16	1.96(∝V')	43(∝V')

gaps are ≈2mm, so capacitance is very large ≈ 1pf/sq cm
with gaps in parallel, NC ≈ 1nF/liter, or ≈ 1μF/cu m

EM towers: NC ≈ 0.2-0.4 nF - a near match to preamp!
Hadronic towers ≈ 10 liters - NC ≈ 10 nF !

SO USE A TRANSFORMER FOR HADRONIC TOWERS!

TRANSFORMER IMPERFECTIONS

Wenzel, 1/19/90
GIN-314, IEEE, S.F.

Ferrite-Core Transformer:

- won't work in large magnetic fields.
- stray primary inductance and stray secondary capacitance.
- associated low impedance lines are bulky and awkward.

Electrostatic Transformer:

- Large DC voltages.
  - + use local decoupling.
  - + split tiles with insulating layer (kapton).
  - + signals are at d.c. ground.
  - + use 2(S-1) voltages ≤V.
  - + voltage across insulating layers is SV/(S-1).
  - + horizontal distribution of voltages minimizes performance degradation from shorts.

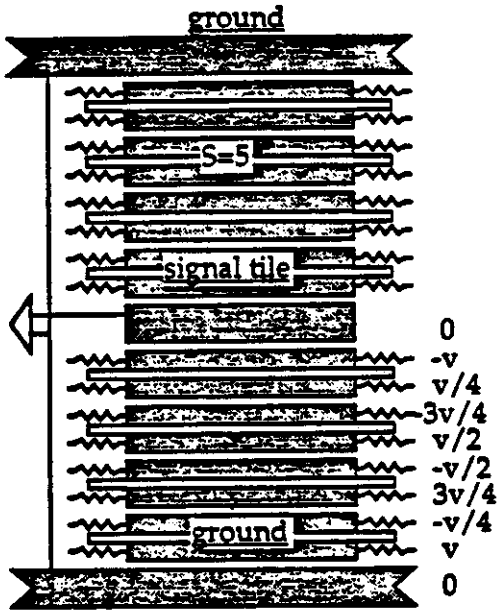

- Crosstalk - coupling of towers through tile to tile capacitance

output capacitance including the effects of crosstalk:

$C_{out} = Cs(1+k)$
where $k = C_c/Cs$
for $k < 0.5$,
$k \approx (2SS+1)(c/6C)$
for $k \geq 0.5$,
$k \approx S\ \mathrm{sqrt}(c/6C)$

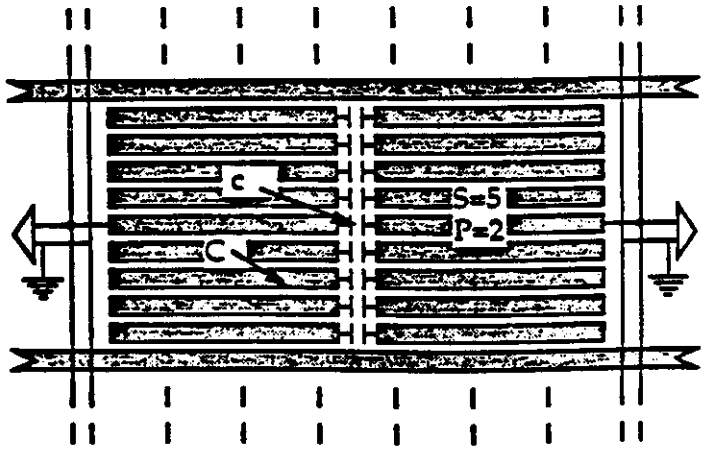

other submodules in parallel

EST MODELS

Wenzel,1/19/90
GIN-314, IEEE, S.F.

Mechanical, electrical and mathematical tests - hardware and SPICE - but no liquid or high voltage.

Model 1.

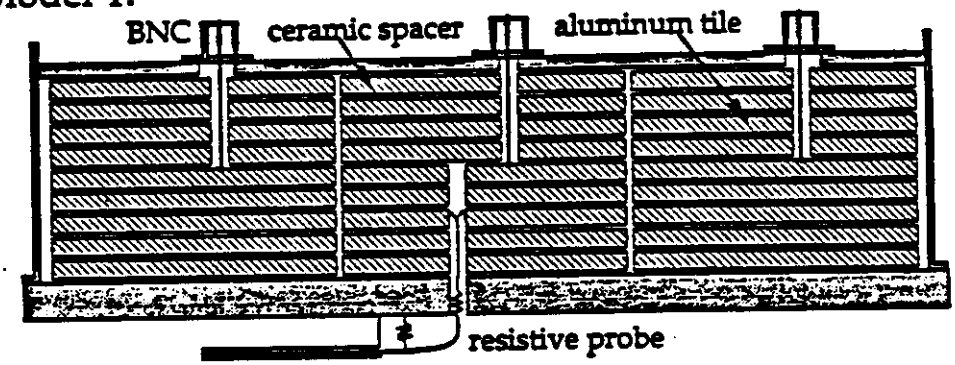

- aluminum tiles and box, nine towers total
- variable S = 1-5; P = 2 (10 gaps maximum)
- tile dimensions: 15 cm x 15 cm x 0.95 cm
- air gaps 0.2 cm; C=100 pf per gap (C_5=40pf!)
- add capacitance (x=6-8) to make $C_S(1+x) \approx 0.3$ nF.
- c/6C=0.015 or 0.03 (tower spacing 0.95 cm or 0.31 cm).
- source probe at bottom; M=1 or 1+2 or .... or 1+2+ ... +S.
- triangular input current pulse: 10ns rise, 100ns total
- TPC integ. preamp (Landis at al. IEEE NS 29 (1), 1982).
- photographed oscilloscope traces (Tektronix 475).

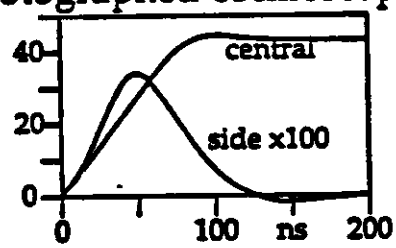

S=4 M=1,2,3,4

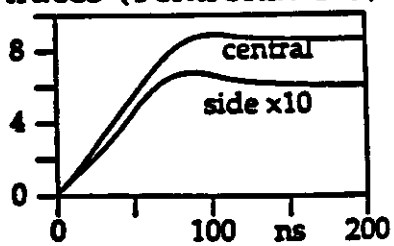

M=1

MODEL 2

Wenzel, 1/19/90
GIN-314, IEEE, S.F.

- tower number, area and tile size, as in Model 1.
- c/6C=0.019 and 0.065 (tower spacing 0.31 and 0.95 cm)
- polypropylene gap 0.15 cm (C≈290 pf/gap)
- top and bottom current source probes
- digital oscilloscopes (Tektronix 2341, 2440 and printer).
- strip line signal ganging (ε=4.3):

	S=5	S=3
C_S ($C_{unloaded}$) nF	0.46(0.046)	1.5(0.15)
tower (ganging) length (cm)	44(33)	46(40)
R_u (ohms)	50	18
L (nHy)	114	51
transit time t_u (t_{loaded}) ns	2.28(7.6)	2.76(9.2)

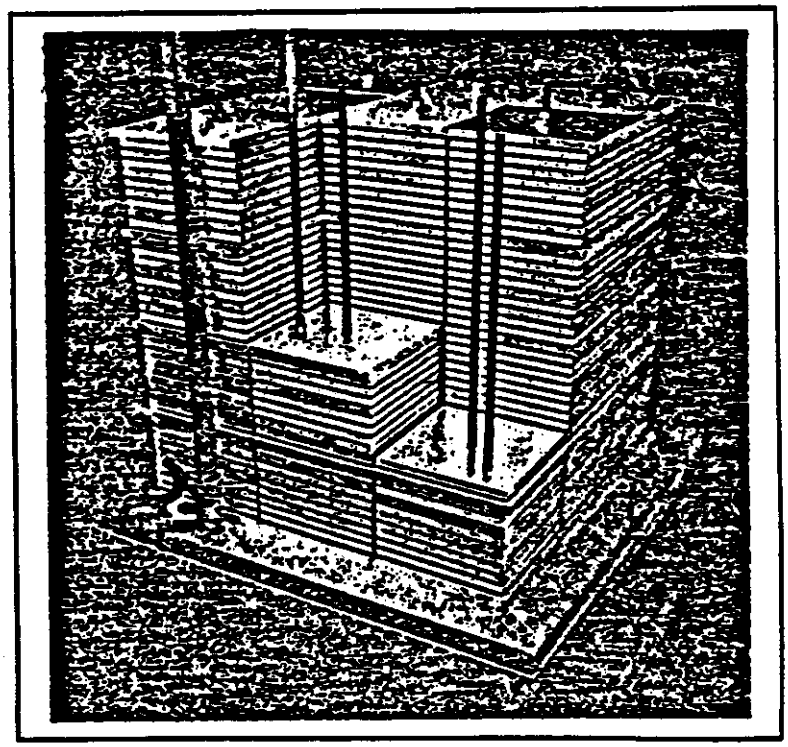

EST-20-inch Deep Aluminum Model

Wenzel, 9/18/89

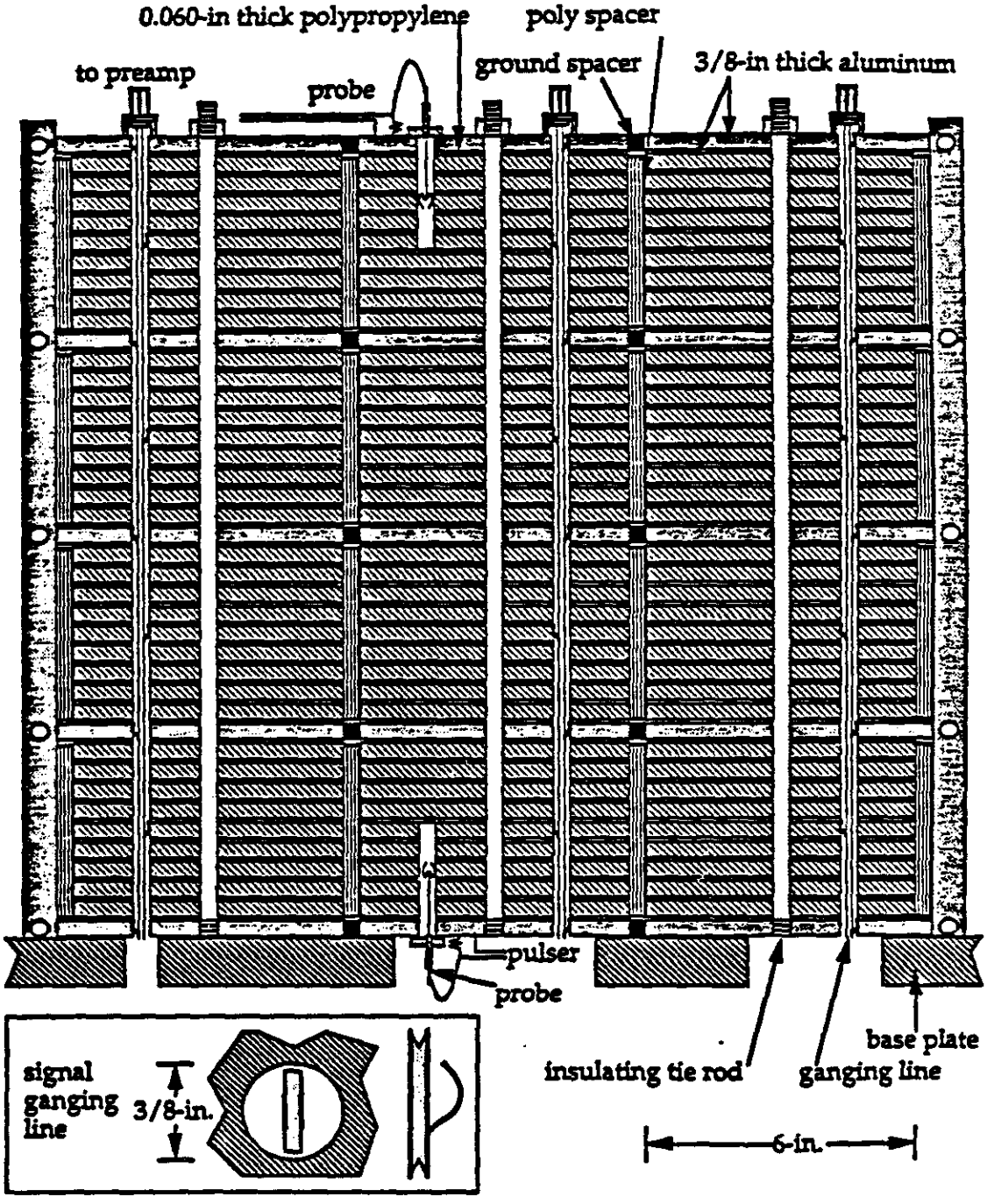

NONUNIFORM GAP EFFICIENCY

Wenzel, 1/19/90
GIN-314, IEEE, S.F.

Net current flow to neighbor depends on the source gap

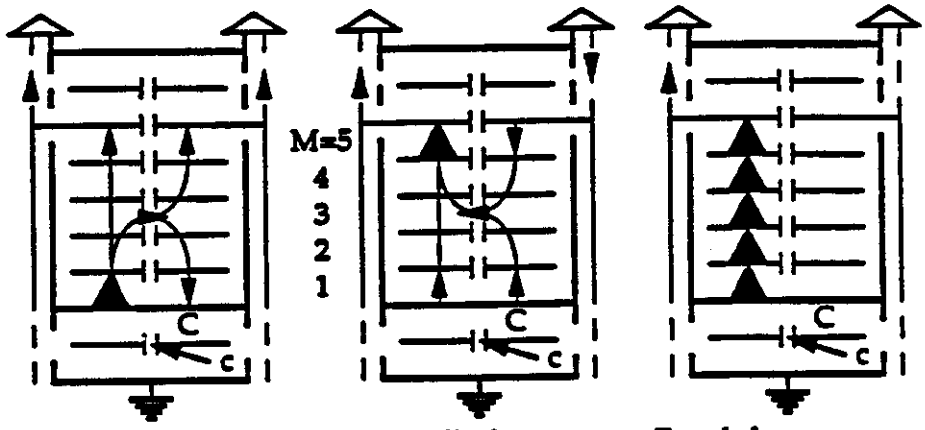

Crosstalk-charge from gap M=1 flows from source-tower into neighbors.

Crosstalk charge from gap M=S (nearest signal tile) has opposite sign.

Equal charges in all gaps conserve charge at each tile - there is no crosstalk.

The total current is conserved at each layer if all neighbors are included. Define gap efficiency E_{SM} for source in M_{th} gap:

E_{SM}=output current in source-tower /total current in all towers

This can vary greatly (e.g. $E_{S5}/E_{S1} > 2$ for 1/8-in spacing).

$\langle(1-E_{SM})\rangle = 0$; (sum is over M)

$(1-E_{SM})_{rms} \approx k \sqrt{[S]/6} \approx (S/6) \sqrt{[Sc/6C]} \neq 0$

Because of varying gap efficiency, charge is delocalized by random fluctuations in gap excitations (If all the charge is collected, this does not cause an energy measurement error).

Let Q_o = output charge for varying source charge Q in all gaps

$(\delta Q_o/Q_o)_{rms} \approx (1-E_{SM})_{rms}(\delta Q/Q)_{rms}/\sqrt{[S]}$.

For S=5, $c/6C \approx 0.02$ (1/8-in tower spacing), $\delta Q/Q_{rms} = 0.5$ gives $(\delta Q_o/Q_o)_{rms} \approx 0.07$ or < 2% per neighbor.

SPICE SIMULATION

Wenzel, 1/19/90
GIN-314, IEEE, S.F.

Tower output current for input-current step-function
S=5, P=8, N=40; M=1,2,3,4,5; $\tau = R_a C_s(1+x) \approx 50 \times 0.5 = 25$ ns;

- current source in top probe
- c/6C = 0.019 (1/8-in tower spacing)

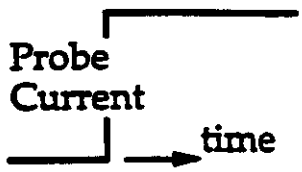

- ganging ripple period:
  for central tower - 26 ns - independent of probe location,
  but dependent on tower spacing.
  for total signal - 18 ns - independent of spacing and probe.
- t_o for top probe is independent of tower spacing
  and ≈ 7 ns earlier than for bottom probe.

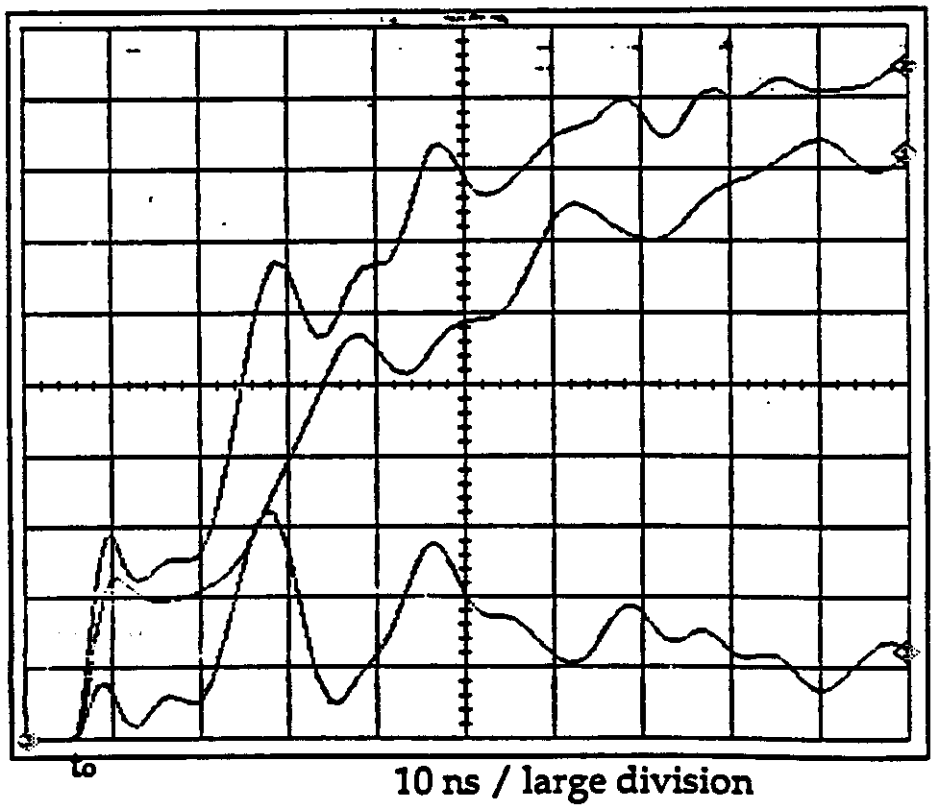

SPICE SIMULATION

Wenzel, 1/19/90
GIN-314, IEEE, S.F.

Tower output current for input-current step-function
S=5, P=8, N=40; M=1,2,3,4,5; $\tau = R_a C_s(1+x) \approx 50 \times 0.5 = 25$ ns;

- current source in top probe
- c/6C = 0.0065 (3/8-in tower spacing)

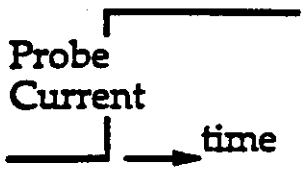

- ganging ripple period:
  for central tower - 22 ns - independent of probe location,
  but dependent on tower spacing.
  for total signal - 18 ns - independent of spacing and probe.
- t_o for top probe is independent of tower spacing
  and ≈ 7 ns earlier than for bottom probe.

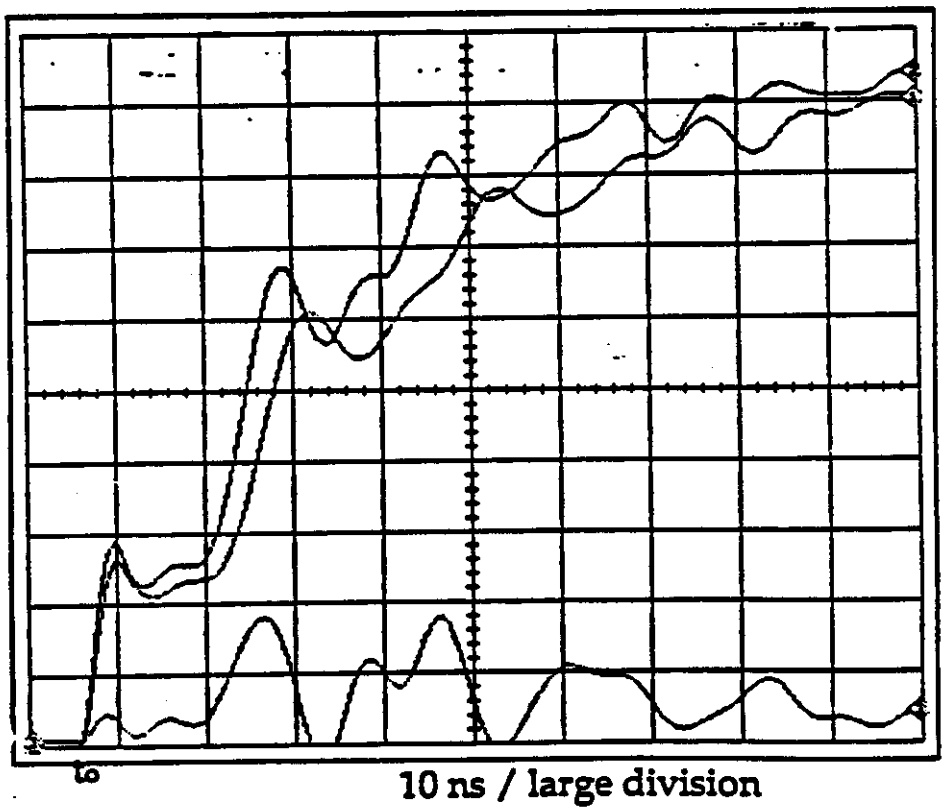

SPICE SIMULATION

Wenzel, 1/19/90
GIN-314, IEEE, S.F.

Tower output current for input-current step-function
S=5, P=8, N=40; M=1,2,3,4,5; $\tau = R_a C_s(1+x) \approx 50 \times 0.5 = 25$ ns;

- current source in bottom probe
- c/6C = 0.019 (1/8-in tower spacing)

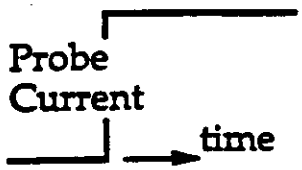

- ganging ripple period:
  for central tower - 26 ns - independent of probe location,
  but dependent on tower spacing.
  for total signal - 18 ns - independent of spacing and probe.
- t_o for bottom probe is independent of tower spacing
  and ≈ 7 ns later than for top probe.

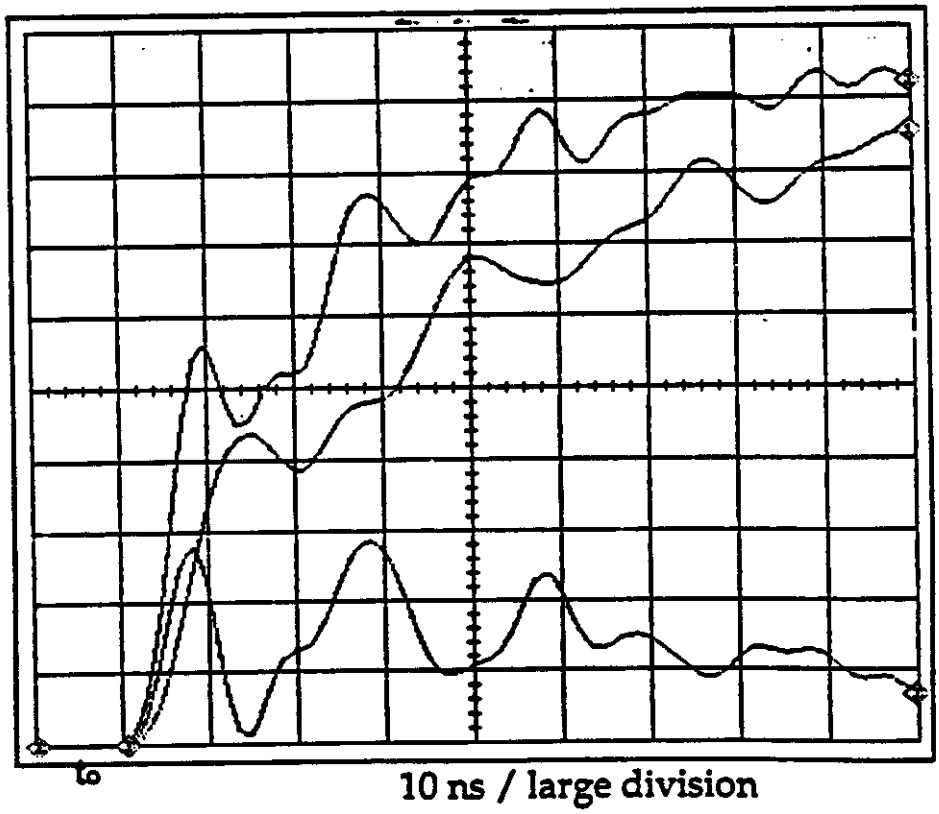

SPICE SIMULATION

Wenzel, 1/19/90
GIN-314, IEEE, S.F.

Tower output current for input-current step-function
S=5, P=8, N=40; M=1,2,3,4,5; $\tau = R_a C_s(1+x) \approx 50 \times 0.5 = 25$ ns;

- current source in bottom probe
- c/6C = 0.0065 (3/8-in tower spacing)

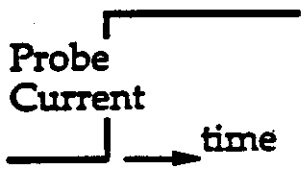

- ganging ripple period:
  for central tower - 22 ns - independent of probe location,
  but dependent on tower spacing.
  for total signal - 18 ns - independent of spacing and probe.
- t_o for bottom probe is independent of tower spacing
  and ≈ 7 ns later than for top probe.

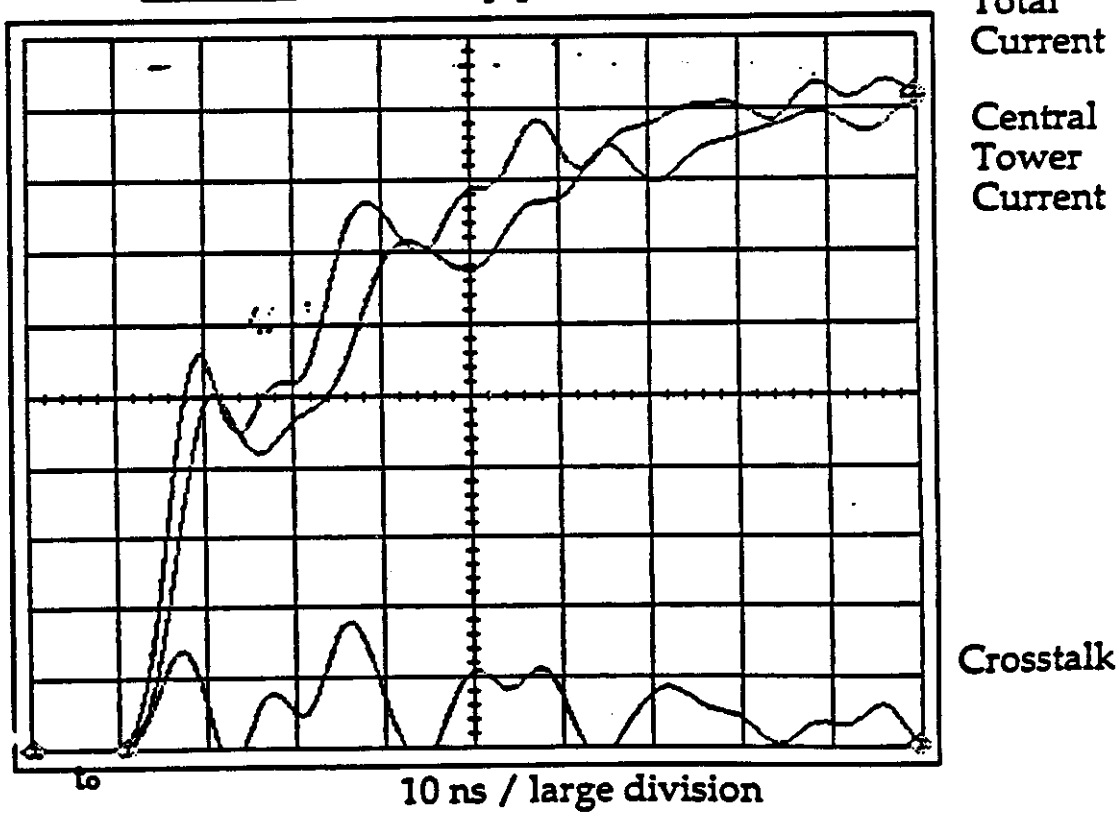

Wenzel, 1/19/90
GIN-314, IEEE, S.F.

MEASUREMENTS ON MODEL 2
using digital oscilloscope

- tower output current for input-current step-function
  S=5, P=8, N=40; M=1,2,3,4,5; $\tau = R_a C_s(1+x) \approx 50 \times 0.5 = 25$ ns;
- current sources in top or bottom probe
- $c/6C = 0.0065$ (3/8-in tower spacing)
- ganging ripple period for central tower
  ≈ 22 ns (SPICE simulation agrees).

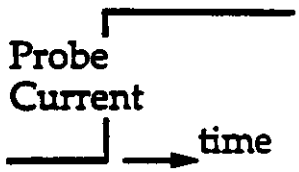

- $\Delta t_o \approx 7$ ns - output from bottom probe delayed relative to top (SPICE simulation agrees).

output current in central tower - top and bottom probes

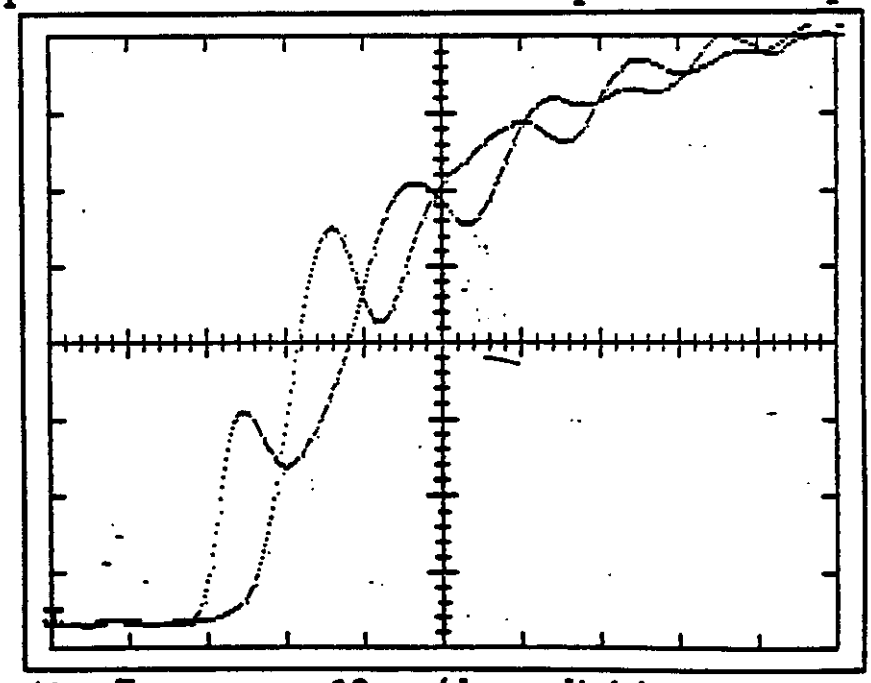

$\Delta t_o \approx 7$ ns 10 ns / large division

MEASUREMENT ON MODEL 2

Wenzel, 1/19/90
GIN-314, IEEE, S.F.

Tower output charge* for triangular probe-current
S=5, P=8, N=40; M=1,2,3,4,5; $\tau = R_s C_s (1+x) \approx 25 \times 0.5 = 12.5$ ns

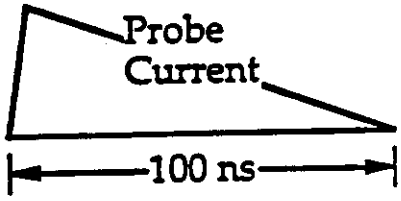

- current source in top probe
- c/6C = 0.0065 (3/8-in tower spacing)
- ganging ripple is barely visible in crosstalk transient (compare measurement using bottom probe)
- rise time (10-90%) is slightly less (≈ 55 ns) for total signal (dashed line) than for central tower.

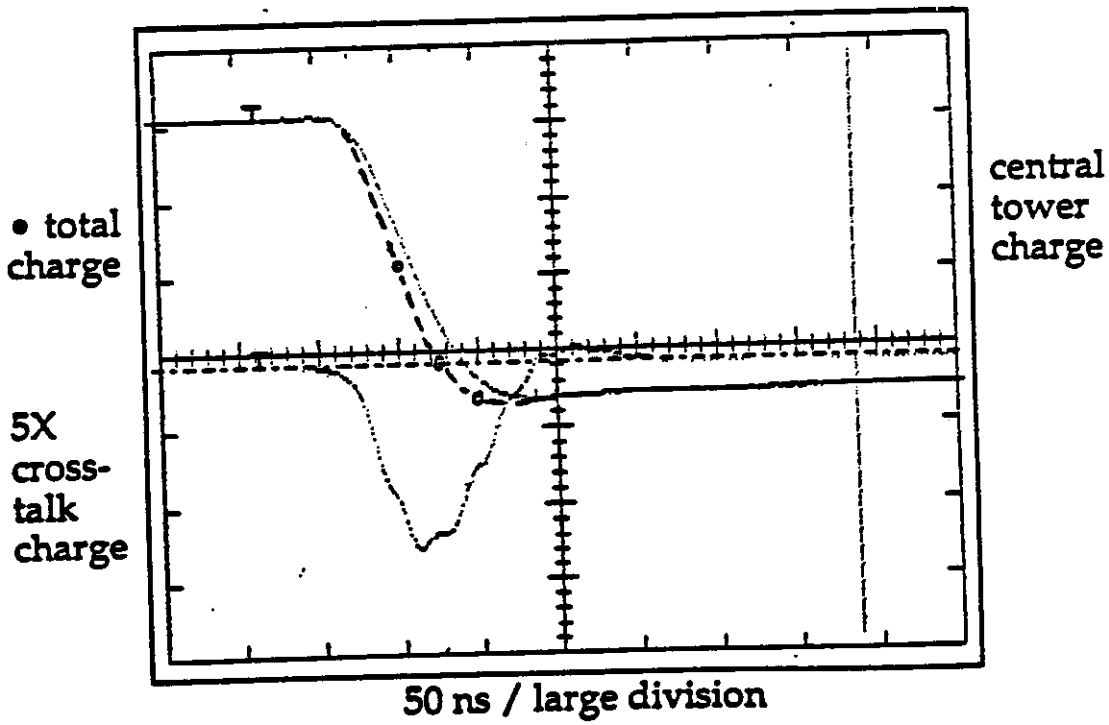

*Integrating preamp:
D.A.Landis, R.S.Adachi, N.W.Madden and F.S.Goulding. IEEEE Transactions in Nuclear Science, Vol. NS-29, No. 1, February, 1982. p573

MEASUREMENT ON MODEL 2

Wenzel, 1/19/90
GIN-314, IEEE, S.F.

Tower output charge* for triangular probe-current
S=5, P=8, N=40; M=1,2,3,4,5; $\tau = R_s C_s(1+x) \approx 25 \times 0.5 = 12.5$ ns

- current source in bottom probe
- c/6C = 0.0065 (3/8-in tower spacing)

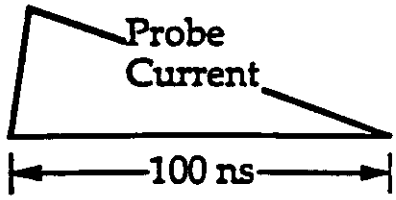

- ganging ripple is barely visible in crosstalk transient
  (compare measurement using top probe)

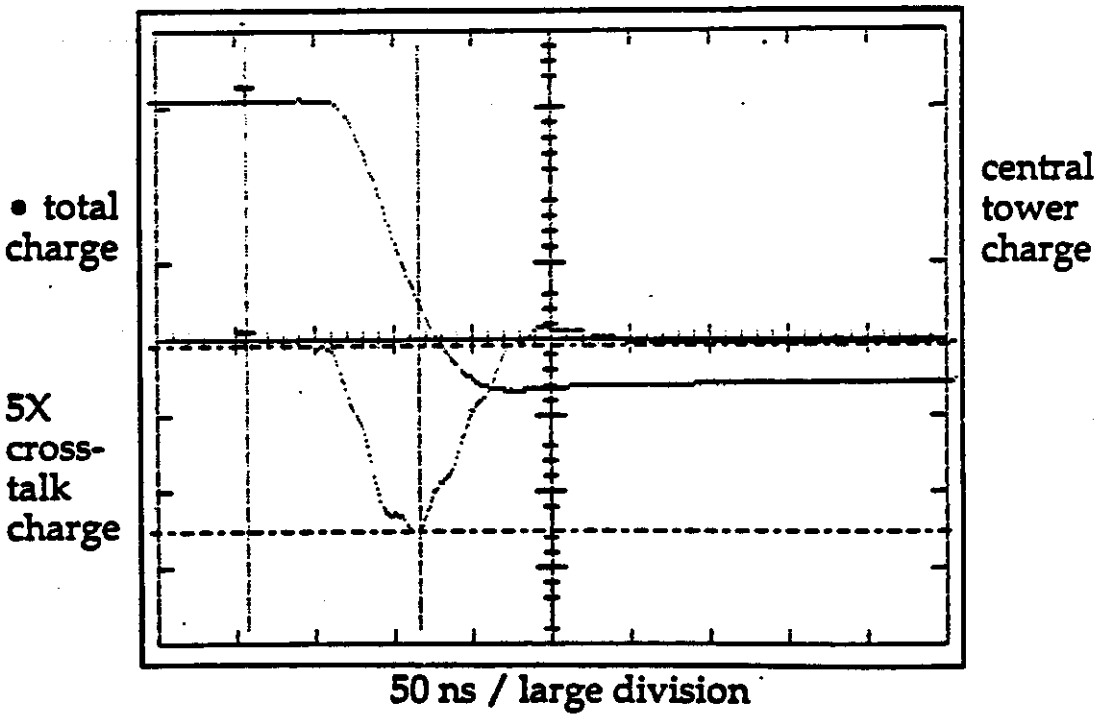

*Integrating preamp:
D.A.Landis, R.S.Adachi, N.W.Madden and F.S.Goulding. IEEEE Transactions in Nuclear Science, Vol. NS-29, No. 1, February, 1982. p573

Wenzel, 1/19/90
GIN-314, IEEE, S.F.

SUMMARY

- Electrostatic transformers can reduce effectively the large capacitance of hadronic towers needed in SSC/LHC calorimetry.

- For charge transfer times in the range 50-100 ns, the impedances of both internal signal ganging lines and external transmission lines are shifted by the EST capacitance transformation to convenient values (≈50 ohms). Series connector and feedthrough inductances do not play a significant role.

- Accumulated high voltage in the tower can be avoided by decoupling between gaps.

- Crosstalk between towers is significant for large transformer ratios, especially with close (≈3mm) spacing. For large values the relative crosstalk contribution to the tower output capacitance is:

$$k = C_c/C_S \approx S\,(c/6C)^{1/2}$$

- In the sum of signals from neighboring towers, charge is conserved; the rise time of the total signal is independent of crosstalk.

- Because of crosstalk the gap efficiencies are not equal. This delocalizes the signal charge by an amount proportional to k. In practical cases the effect is small.

LBL-28511

The Electrostatic Transformer

J. Colas, M. Pripstein, and W.A. Wenzel

Physics Division
Lawrence Berkeley Laboratory
University of California
Berkeley, CA 94720

February 1990

This work was supported by the Director, Office of Energy Research,
Office of High and Nuclear Physics, Division of High Energy Physics
of the U. S. Department of Energy under Contract No. DE-AC03-76SF00098.

THE ELECTROSTATIC TRANSFORMER[1]

J.Colas[2], M.Pripstein and W.A.Wenzel,
Lawrence Berkeley Laboratory, Berkeley, CA 94720

Abstract

The electrostatic transformer (EST) has been developed to match the large capacitance hadronic signal towers of liquid ionization calorimeters to relatively low capacitance, low noise preamplifiers. The intrinsically fast internal impedance transformation by the EST preserves the fast rise time required for effective calorimetry in the high rate environment of the SSC/LHC. Another advantage of the EST over an external ferrite-core transformer (FTC) is that the former is unaffected by the large magnetic field required in most detector configurations. The performance of the EST is limited primarily by crosstalk to neighboring towers, which delocalizes the signal and degrades the signal to noise ratio. In practical applications both these effects can be made small. To aid in the evaluation and design of useful EST's we have studied an aluminum model of a hadronic tower section of typical dimensions. The measurements on the model agree well with calculations using a simple electrical model.

I. LIQUID IONIZATION CALORIMETRY AT THE SSC

In liquid ionization sampling calorimetry the charge is collected using high voltage across uniform sensitive gaps of liquid. These alternate with uniform plates of high Z absorber. Since the signal is proportional to the energy lost, the sensitivity is determined primarily by the geometry, calibration is relatively easy and long term stability is excellent. Other advantages of the ion chamber technology are the short intrinsic rise time of the current pulse and relative insensitivity to radiation damage.

The most significant limitations of the technology derive from the large source capacitance coupled with an intrinsically small ionization signal. The SSC/LHC needs for both fast signal response and excellent energy resolution are especially challenging because the frequent sampling needed for good energy resolution tends to require larger capacitance. Typical hadronic towers extend for two absorption lengths or ≈0.5m in depth with total capacitance ≈10nF. Unless this is reduced, the preamp impedance as well as the inductances associated with cabling, feedthroughs and other connectors can limit significantly the charge transfer time.

Larger capacitance also means more noise. To limit the power and cost of electronics the preamp capacitance per tower must be no more than a few hundred pf; and since the noise is minimized by matching the source capacitance to that of the preamplifier, noise reduction provides a second motivation for reducing the effective output capacitance of the detector.

This work is part of a general effort by the Warm Liquid Calorimetry Collaboration (WALIC)[3] to study room temperature liquids (TMP/TMS) as alternatives to cold liquid argon as sensitive media in sampling calorimeters for the SSC/LHC.

II. TRANSFORMER MATCHING

Alternative designs for a hadronic tower are shown schematically in Figure 1. In both cases the absorbing electrodes are separated by liquid sensitive gaps. Ionization electrons produced by shower particles (dashed diagonal trajectories) are collected with the help of a large voltage gradient (≥10kV/cm). The absorber includes

both the ground plates and the conducting tiles, which define the cross sectional areas of the individual towers.

Otherwise the designs are very different. Figure 1a shows the traditional means of capacitance matching with an external transformer[4]; within the tower all the signal gaps are in parallel. Figure 1b shows an alternative in which subsets of gaps within the tower are in series[5,6]. As seen from the preamplifier this performs an impedance transformation like that of the external ferrite-core transformer (FCT). Because the internal transformation makes direct use of the pulse-energy in the high voltage sensitive gaps, we identify it as an electrostatic transformer (EST).

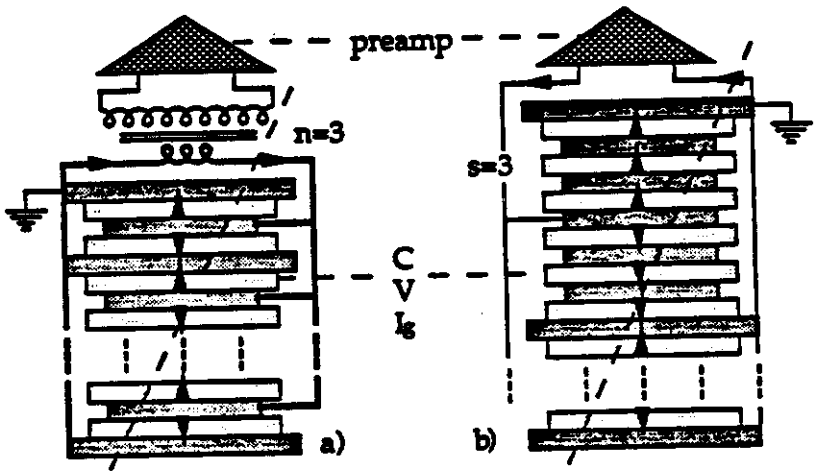

Figure 1. Schematic representation of capacitance matching for a hadronic tower. High voltage connections are not shown. I_g is the ionization current in the g^{th} gap. V and C are the d.c. voltage and capacitance per gap, respectively. The arrows show the directions of current flow. In a) all N gaps are connected in parallel; matching is achieved with a ferrite-core transformer with turns ratio n=3. b) shows an electrostatic transformer with P parallel subtowers of S=3 gaps in series (N=SP).

Table 1 below compares these two types of transformers, each assumed to be ideal.

Table 1. Comparison of ferrite-core and electrostatic transformers used with parallel and series-parallel connected hadronic towers, respectively. Parameters are defined in Figure 1.

Parameter	FCT(Primary)	FCT(Secondary)	EST(Series-Par.)
transformer ratio	n		S
capacitance	NC	NC/n^2	$NC/S^2=PC/S$
signal current	ΣI_g	$\Sigma I_g/n$	$\Sigma I_g/S$
total d.c. voltage	V	----	SV

As an example of the use of the EST, a tower with 40 gaps of 250pf each has a total capacitance of 10nF if all gaps are connected in parallel, but only 0.4nF if there are 8 parallel sets of 5 gaps each in series.

Table 1 implies that the d.c. voltages in adjacent gaps of the EST are connected in series. This is conceptually straightforward, but requires very high voltage for an EST of large S. In various alternative designs[5] the gaps are decoupled individually,

so that the maximum voltage is no greater than the constant voltage V across each gap. The example shown in Figure 2 uses resistively decoupled high voltage on all but the signal tiles, which are at d.c. ground. Signal decoupling uses the capacitance between tiles on opposite sides of the insulators. The voltage difference across each insulator is VS/(S-1).

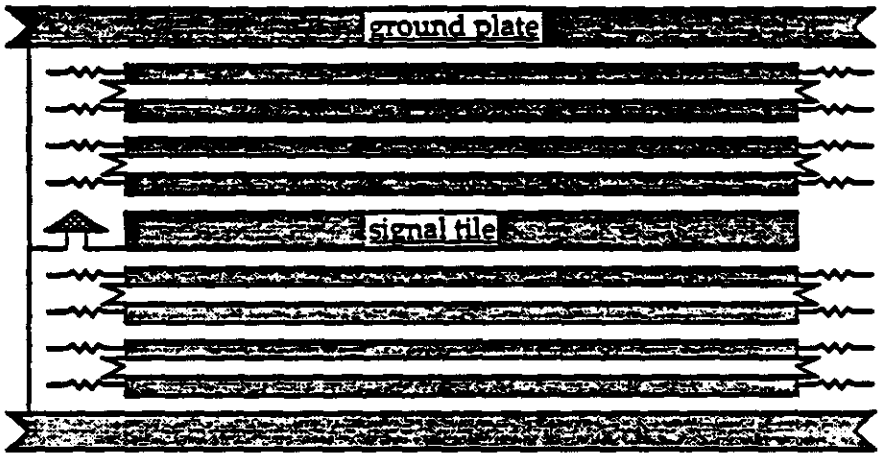

Figure 2. Schematic of two subsections of tower with an electrostatic transformer of ratio S=3. Absorbing signal tile is at d.c. ground. High voltages, decoupled by large resistances, are supplied to the half-tiles, which are separated by thin insulating layers.

III. SIGNALS FROM HADRONIC TOWERS

The small signals from the gaps of the relatively large volume (≥10 liter) hadronic towers must be summed and transported to preamplifiers which are not necessarily close to the source.

A. Ionization current and signal risetime.

Figure 3a shows the time dependence of the electron current in a uniformly illuminated calorimeter gap. In liquid argon the drift velocity is nearly independent of, and in the organic liquids (TMP, TMS) it is nearly proportional to the voltage gradient. For TMP or TMS at the SSC/LHC, the charge collection time T will be ≤100ns. Because the drift of free electrons begins instantaneously, the intrinsic risetime of the ionization current pulse is very small. Preserving this valuable feature in the amplified signal, however, poses some severe challenges for hadronic towers of large capacitance[4][6].

Figures 3b and 3c show the signal paths for the FCT and the EST. The capacitive feedback of the preamp gives a resistive input impedance R_s[4] to damp the signal current with time constant τ. Without a transformer an NC=10nf tower would need a 2.5 ohm preamp input resistance for a pulse rise time 2τ=50ns (10-90%). If an FCT is used the signal rise time is especially vulnerable to inductance associated with ganging, connectors and transformer leakage in the large capacitance primary circuit ($L_{crit}=R^2C/4$=19nHy). For simplicity we neglect the L's, but include C_s, the stray capacitance of the transformer secondary. For the FCT and EST:

$$\tau_{FCT}=R_a[(C_S+C_x)/n^2+C_a+C_s] \qquad (1)$$
$$\tau_{EST}=R_a(C_S+C_x+C_a)$$

where $C_S=NC/S^2$ (S=1 for FCT), and C_x includes signal ganging and, depending on the configuration, other capacitances external to the tower. In the Helios experiment[7] an FCT at the tower output is used to match the tower capacitance to a low capacitance preamp. If the FCT and preamp are connected to the tower by a transmission line which is short, i.e., with transit time $t_t<<\tau$, then C_x includes the transmission line capacitance $C_t=t_t/R_t$ (see Figure 3). If for the FCT(EST) $n^2R_t \geq R_a$ ($R_t \geq R_a$) then $C_t<<C_S$, and the transmission line does not greatly affect the design and operation.

An important limitation of the FCT, however, is that it won't work in high magnetic fields. If a long transmission line ($t_t \geq \tau$) is used for this reason and/or to make the preamps more accessible for service, then the signal risetime is preserved only if the transmission line is terminated; i.e., $R_t=R_a$. This condition provides a simple scaling law for the transmission line capacitance; i.e., $C_t/C_\tau=t_t/\tau$, where $C_\tau=C_S(1+x)$ is the relevant capacitance on the tower side of the transmission line, and we define $x=C_x/C_S$. For the NC=10nF tower with τ=25ns, R_{tFCT}=2.5 ohms; for an S=5 EST R_{tEST}=62.5 ohms, in a much more convenient range.

For the termination to be effective it is necessary also that C_a not be too large; i.e., for the EST, $R_aC_a<<\tau$; for the FCT, $R_aC_a(1+s)<<\tau$, where $s=C_s/C_a$.

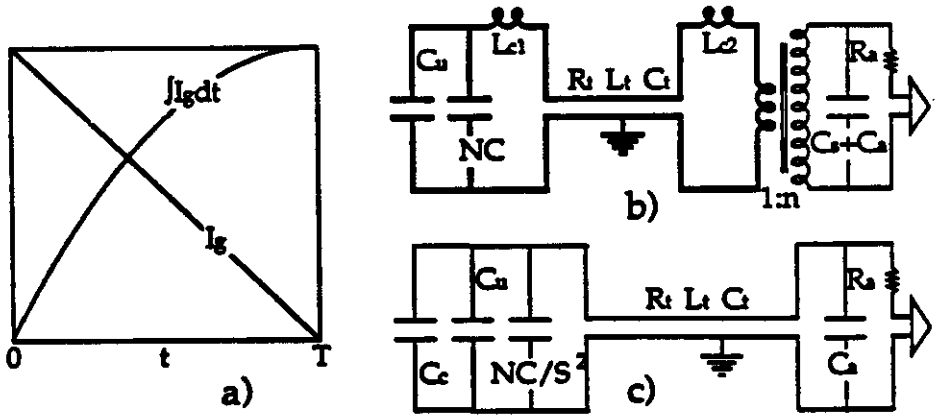

Figure 3. a) shows the ionization current and its integral from a sensitive gap uniformly illuminated at t=0. T is the charge collection time. b) shows schematically the components which can contribute significantly to the charge transfer time if an FCT is used for capacitance matching at the preamp. NC is the paralleled tower-gap capacitance, C_u, C_t, and C_s are for the internal signal ganging line, the transmission line and the stray capacitance of the FCT, respectively. C_a is the input capacitance and R_a the input resistance of the preamp. Bold lines indicate large signal currents; the L_c's are stray inductance from feedthroughs, signal connections and transformer leakage. High voltage decoupling capacitors are not shown. c) shows the corresponding parameters for the EST, for which C_c is the crosstalk contribution to the output capacitance.

B. Signal ganging

In order that the tower gaps be sampled uniformly, the differences in the signal arrival times must be small compared with the pulse shaping time. If we assume that, as a practical design feature, the tower signal is extracted from one end, then we require that $10ns=t_g<<2\tau=50ns$, where t_g is the transit time of the signal ganging line. We require also, to limit the capacitance, that the ganging line capacitance is a small fraction g of C_S, then all the ganging line parameters are effectively determined by g, C_S, the dielectric constant ε, the tower depth l and the velocity of light v. For the unloaded (subscript u) and capacitatively loaded (g) ganging line these are:

$$C_u=gC_T;\ t_u=(l/v)(\varepsilon)^{1/2};\ L_u=(t_u)^2/C_u=(l/v)^2(\varepsilon/gC_S);\ R_u=(l/vgC_S)(\varepsilon)^{1/2} \qquad (2)$$
$$C_g=C_S(1+g);\ t_g=t_u[(1+g)/g]^{1/2};\quad L_g=L_u;\qquad R_g=R_u[g/(1+g)]^{1/2}$$

For ε=2; g=0.1, l=0.5m, we find t_g=7.8ns; $L_g(nHy)=56/C_S(nF)$; $R_g(ohms)=7.1/C_S(nF)$. Hence, independent of tower area or choice of FCT or EST, an acceptably small transit time is achieved with only a 10% increase in tower capacitance. But for a 10nF tower the ganging-line inductance for an FCT is a very low 0.1nHy/cm.

C. Effect of crosstalk on tower output capacitance

Figure 4 shows schematically the sources of crosstalk between a central and eight surrounding towers. A fraction of the charge produced in each central gap is coupled to the four side towers, which are similarly coupled to the corner towers.

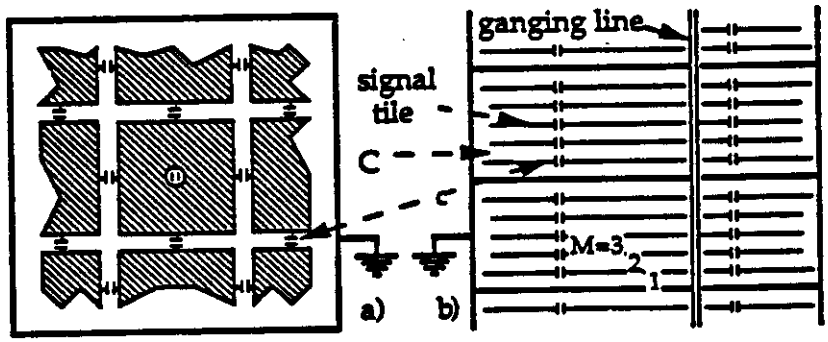

Figure 4. Plan and elevation schematics showing sources of crosstalk between towers of an EST with S=3. Each calorimeter module of many towers is in a grounded container. M is the gap number within a subtower; C is the capacitance of each gap, and c is the coupling, assumed to be constant, of each tile to that of a side tower. Within each tower the signal tiles are summed along a low impedance ganging transmission line, shown here for the central tower only.

For an EST the tower output capacitance C_o includes three important terms:

$$C_o=C_S+C_c+C_u=C_S(1+k+g) \qquad (3)$$

where $C_c=kC_S$ is from crosstalk and $C_u=gC_S$ is discussed in III.*B.* above. Table 2 gives an exact calculation of k for central and side towers (i.e., ignoring presence of

corners). The first order (in c/C) expression for C_c gives $k=(Kc/6C)(2S^2+1)$, valid for $k\leq 0.5$. For $k\geq 0.5$, the most interesting range, a good fit is obtained with $k=S(Kc/6C)^{1/2}$.

Table 2. Crosstalk fraction, $k=C_c/C_S$ for central and nearest-neighbor towers.

S	(Kc/6C)=	0.01	0.02	0.03	0.04
1		0.030	0.059	0.088	0.117
2		0.087	0.168	0.245	0.317
3		0.175	0.327	0.459	0.576
4		0.287	0.510	0.690	0.842
5		0.412	0.699	0.915	1.087
6		0.545	0.882	1.121	1.304
7		0.679	1.053	1.305	1.494
8		0.809	1.210	1.470	1.659
9		0.935	1.354	1.616	1.805
10		1.054	1.484	1.747	1.934

D. Effect of crosstalk on gap efficiency and preamp noise

Crosstalk distributes the signal among neighboring towers. If the tiles are coupled only to neighboring tiles, the total signal charge is conserved among all towers; but the signal of each tower depends on the source-gap and varies with time. For source-charge Q_{SM} deposited at time t=0 in the M^{th} gap of a subtower of S gaps the sum of all tower currents is:

$$I_{aSM}(t) = (Q_{SM}/S\tau)e^{-t/\tau} \qquad (4)$$

where τ is defined in (1). To first order in c/C the current $i_{aSM}(t)$ in a side tower is:

$$i_{aSM}(t) = I_{aSM}(t)(c/6C)[(S^2-1-3M^2+3M)+(2S^2+1)(1-t/\tau)/(1+x)] \qquad (5)$$

The corresponding integrated preamp output charges are:

$$Q_{aSM}(t) = (Q_{SM}/S)(1-e^{-t/\tau}) \qquad (6)$$
$$q_{aSM}(t) = (Q_{SM}/S)(c/6C)[(S^2-1-3M^2+3M)(1-e^{-t/\tau})+(2S^2+1)(t/\tau)e^{-t/\tau}/(1+x)]$$

where x is defined in III.*A.* above. The charges in the central and side towers are:

$$Q_{aSM\text{-cent}}(t)=Q_{aSM}(t)-Kq_{aSM}(t) \qquad q_{aSM\text{-side}}(t)=q_{aSM}(t) \qquad (7)$$

The M-independent term of $q_{aSM}(t)$ has the same sign as $Q_{aSM}(t)$, its amplitude is reduced by the external capacitance x, and it vanishes at $t=\infty$. The M-dependent term is independent of the external capacitance, has a time dependence similar to that of $Q_{aSM}(t)$, and vanishes in the average over M. This last feature is general, a direct consequence of the tower symmetry; i.e., if all gaps are uniformly excited, no net charge is produced on the internal tiles, and there is no crosstalk.

Important consequences of this average condition are first, that τ does not depend on C_c, although the latter can be a significant part of C_o; and second, that the effect of the crosstalk on preamplifier noise depends on the application. When the tower signals are separately recorded, crosstalk related noise is included, because the

gap signals are incoherent. But if, as is common, many tower signals are summed coherently for a trigger, the coherent noise among these cancels.

The gap-efficiency E_{SM} for each gap is defined to be the normalized charge output from the central tower at $t=\infty$ divided by the total charge from all towers.

$$E_{SM} = 1-Kq_{aSM}(\infty)/Q_{aSM}(\infty) = 1-(Kc/6C)(S^2-1-3M^2+3M) \qquad (8)$$

The first form on RHS is general; the last, from (6), is to first order in c/C.

For an arbitrary time dependent source-function the time dependent preamp charges are obtained by folding. Figure 5 shows examples for triangular distributions (Figure 3a) of different durations.

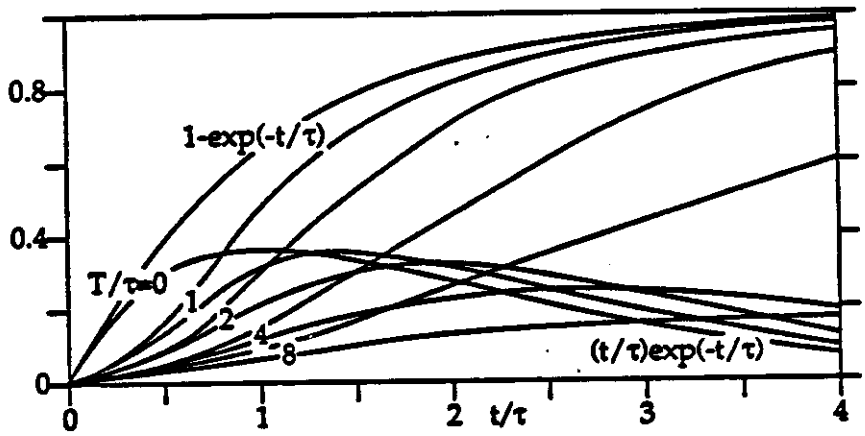

Figure 5. Time dependence of terms describing crosstalk-charge for triangular source functions (Figure 3a) of length T. τ is the time constant defined in (7). Amplitudes are unnormalized.

IV. MODELS OF EST

To evaluate more carefully the electrical and mechanical properties of a calorimeter based on the EST, we have used both mechanical-electrical models and computer-simulation.

A. Aluminum model and computer simulation program SPICE

Figure 6 shows an aluminum model of nine towers assembled inside a grounded box. The central tower was surrounded by four nearest neighbors (sides) and four next nearest neighbors (corners). The dimensions of the aluminum tiles were 6"x6"x3/8". Within the towers the (air) gaps between tiles were set at 0.078" by ceramic spacers.

In each tower the signal from the central tile, which collects charge from both subtowers, was accessible on a rod in a vertical hole through the upper subtower. With access from the top the numbers of tiles between each signal tile and the two ground plates which formed the top and bottom boundaries were changed to vary S. For S=5 (10 gaps), the maximum available, the total depth was approximately one-

fourth that of a high-Z tower of two absorption lengths thickness. The crosstalk capacitance c was varied by changing the tower spacing, which was either 0.125" or 0.25" of air.

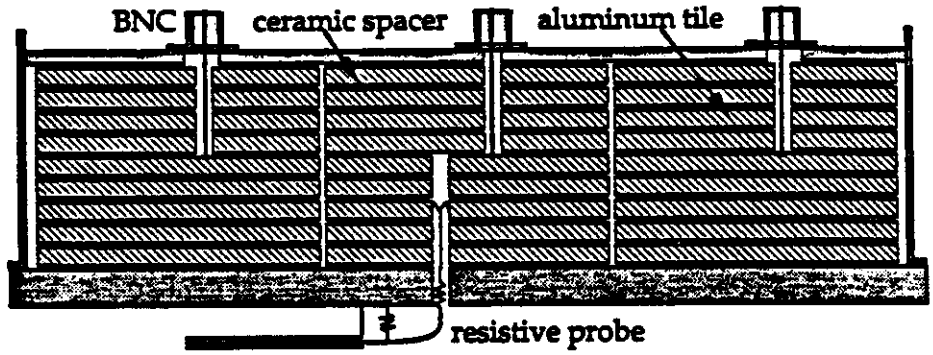

Figure 6. Assembly of the nine-tower aluminum model for S=5. Dimensions are given in the text.

The source current waveform was triangular, of total length 100ns and risetime ≤10ns (Figure 3a). In practice the probe current flowed between a given tile and ground; the effect of a current source in a single gap was obtained from differences. For a variety of conditions the time dependent integrated charge was detected using charge sensitive integrating preamps[8] of 50 ohms nominal input impedance. These monitored the central tower and one other; the seven towers without preamps were terminated in 50 ohms. The measurements were made from photographed traces of a Tektronix 475A Oscilloscope.

Examples of the two crosstalk terms [$q_{aSM}(t)$ in (6)] are illustrated in Figure 7, which shows the charges on the central and one side tower when all gaps or a single gap are excited.

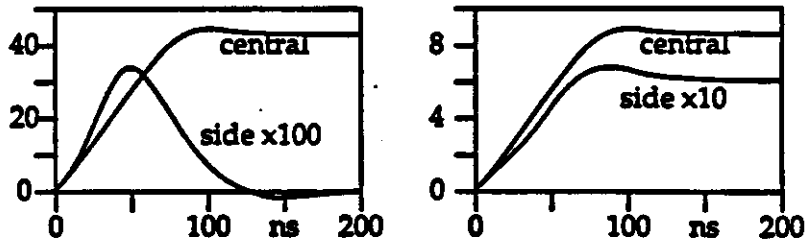

Figure 7. Observed time dependent integrated output currents from the central and a neighboring (side) tower for S=4. and Kc/6C=0.0158. In the left figure all gaps (M=1-4) are excited; at the right only one gap (M=1) is excited. The relative amplitudes are preserved in the vertical scales.

Figure 8 shows the configuration for the simulation program SPICE. The coupling capacitance c was calculated from first principles, i.e., from tower spacing and tile areas. The simulation includes only the central and side towers, omitting crosstalk to the corners and to the surrounding ground box. With large gaps around the outside, the latter effect is negligible. Measurements on the aluminum model for the closest tower spacing (1/8") show that for this 'worst case' the signals from the

corner towers are ≈10% of those from the side towers. Without the next nearest neighbors in the simulation, therefore, the total crosstalk charge decreases by ≈1%.

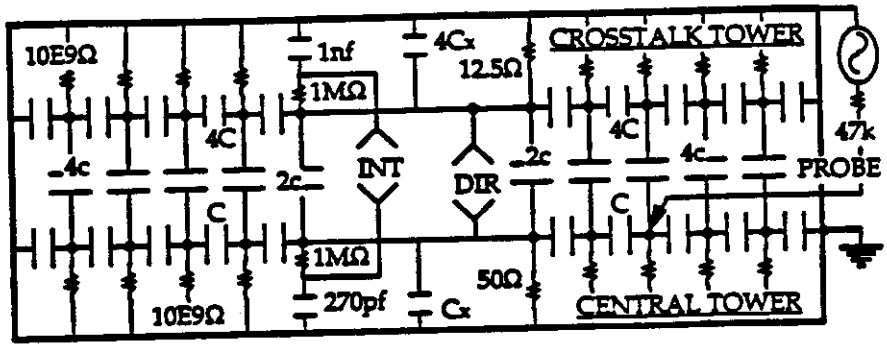

Figure 8. Equivalent circuit used in SPICE calculations for transformer ratio S=5. The crosstalk coupling, stray capacitance and the tower and preamp parameters are combined for the K(=4) nearest neighbors. C_x is the external (including preamp) capacitance. The input voltage pulse on the PROBE is triangular. The voltages at DIR are proportional to the input currents to the preamps. INT voltages are proportional to the outputs from perfect integrating preamps.

B. Comparisons of measurements and SPICE calculations

Table 3 compares measurements on the aluminum model with SPICE calculations; these are generally in excellent agreement. The agreement in the gap-efficiency E_{SM} measurements shows that the tile to tile couplings are relatively

Table 3. Comparison for S=3 and 5 and for tower spacings of 1/8" and 1/4" of measurements on the aluminum model with calculations using SPICE. The source current is shown in Figure 3a; measured and calculated parameters are defined in the text. K=4; C=100pf; normal sampling time =200ns.

tower spacing	M	1/8"(Kc/6C=0.0317) meas.	calc.	1/4"(Kc/6C=0.0158) meas.	calc.
S=5:					
output capacitance C_o(pf)		85	84	69	69
gap efficiency E_{SM}	1	0.56	0.56	0.72	0.72
	2	0.65	0.65	0.76	0.78
	3	0.82	0.83	0.88	0.92
	4	1.15	1.20	1.12	1.12
	5	1.81	1.76	1.52	1.46
transient-peak time(ns)	1-5	35	41	40	43
normalized amplitude	1-5	0.054	0.034	0.032	0.019
S=3:					
output capacitance C_o(pf)		104	104	90	89
gap efficiency E_{SM}	1	0.79	0.80	0.87	0.89
	2	0.94	0.94	0.95	0.97
	3	1.27	1.26	1.18	1.14
transient-peak time (ns)	1-3	70	72	70	71
normalized amplitude	1-3	0.022	0.017	0.013	0.009

uniform. During the time between the source pulse and normal sampling (200ns), a few per cent of the initially transferred charge was reclaimed by the resistive input PROBE. Since this effect is M-dependent, it distorts the gap efficiencies in the Table; by correcting for this and summing the signal from all nine towers, we find that charge is conserved to ≈1%. The measurements of tower output capacitance C_o include some stray capacitance. Known contributions of ≈ 6pf from the signal rod and BNC output connector are included in the calculations, which agree embarrassingly well with the measurements.

External capacitance was added in parallel with the inputs to the preamps in order to bring the time constant τ of the system into a range appropriate for realistic towers four times as deep. The crosstalk transient term, therefore, was suppressed by relatively large values of x (≈ 6-8). Measurements in the Table are given only for full subtower excitation (all gaps), which maximizes the visibility of this term (Figure 7).

V. CHARGE DELOCALIZATION BY CROSSTALK

Although the signal charge from a tower is on the average proportional to the charge released in that tower, the M-dependence of the gap efficiency E_{SM} means that random fluctuations in the gap-excitations will introduce uncertainties in the transverse charge distribution. From (8) the t→∞ output charges in all towers Q_{aS} and in all side towers Kq_{aS} produced by charges Q_{SM} in the gaps of the central tower are:

$$Q_{aS} = \Sigma\, Q_{SM}/S \qquad Kq_{aS} = \Sigma\, Q_{SM}(1-E_{SM})/S \tag{9}$$

where the sums are over M. Assuming that on the average Q_{SM} and fluctuations δQ_{SM} are independent of M with average values $\langle Q_{SM}\rangle = Q$ and $\langle \delta Q_{SM}\rangle = 0$, we obtain from (9), $\langle Q_{aS}\rangle = Q$, $\langle q_{aS}\rangle = 0$ and:

$$(Kq_{aS}/Q_{aS})_{rms} = (\delta Q/Q)(1-E_{SM})_{rms}/S^{1/2} = F(S)\delta Q/Q \tag{10}$$

where we define $F(S) = (1-E_{SM})/S^{1/2}$ and $\delta Q = \delta Q_{SMrms}$. Exact (without the corner towers) calculations of F(S) are given in Table 4. For k≥0.5, F(S) ≈ k/6 (see Table 2). For S=5 and Kc/6C=0.02, (E_{55}/E_{51}=2.3), Table 4 gives F(S) = 0.143; i.e., if $\delta Q/Q = 0.5$, only 7% of the charge is delocalized; less than 2% appears in each side tower.

Table 4. Delocalization of charge by crosstalk. Tabulation is of $(1-E_{SM})_{rms}/S^{1/2}$ with 1≤M≤S.

S	(Kc/6C)	0.01	0.02	0.03	0.04
1		0	0	0	0
2		0.020	0.039	0.057	0.074
3		0.040	0.075	0.106	0.134
4		0.061	0.111	0.151	0.185
5		0.082	0.143	0.189	0.226
6		0.102	0.170	0.220	0.258
7		0.121	0.194	0.244	0.281
8		0.138	0.213	0.263	0.299
9		0.153	0.229	0.278	0.313
10		0.166	0.242	0.290	0.324

VI. CONCLUSIONS

The electrostatic transformer is competitive with ferrite-core transformers in reducing the large capacitances inherent in the hadronic towers needed for SSC calorimetry. Advantages of the EST are that it can preserve the intrinsically fast rise of the ionization pulse, that it is insensitive to magnetic fields and that for preamps located far from the towers it matches a transmission line of convenient impedance. EST performance is degraded primarily by crosstalk between neighboring towers, which delocalizes the signal from the tower of origin. For practical cases this effect is estimated to be small.

Both mechanical and electrical properties of the EST have been studied by testing an aluminum model of nine short towers with transverse dimensions typical of hadronic towers for the SSC/LHC. The performance of the towers is quantitatively predictable from a few geometrical parameters including volume, transformer ratio (number of gaps in series) and the spacing between neighbors. The agreement with electrical measurements has shown that the performance of an EST can be predicted using a simple electrical circuit like the one in Figure 8, which can be computed accurately by SPICE or other methods.

The fabrication and operation of the model have revealed some of the problems of tower and module assembly and signal ganging. Tests are underway using a model with towers of full depth.

References

[1]. This work was supported by the Director, Office of Energy Research, Office of High and Nuclear Physics, Division of High Energy Physics of the United States Department of Energy under Contract No. DE-A C03-76SF00098
[2]. Permanent address: L.A.P.P., Annecy-le-Vieux, 74019, France.
[3]. LBL Group A Physics Note #971, 9/87.
[4]. V. Radeka and S. Rescia. Nucl. Instr. Meth. in Phys. Res., A265 (1988) 228-242
[5]. J.Colas and W.A.Wenzel. "Electrostatic Transformers for Large Towers". LBL-27236. Presented at the Workshop on Calorimetry for the SSC, Tuscaloosa, AL, March 13-17, 1989, and to be published in the Proceedings.
[6]. J. Colas. "Speed of Response, Pile-up, and Signal to Noise Ratio in Liquid Ionization Calorimeters". LBL-27328. Presented at the Workshop on Calorimetry for the SSC, Tuscaloosa, AL, March 13-17, 1989, and to be published in the Proceedings. Also, LAPP-EXP-89-13, November, 1989. Submitted to the proceedings of the ECFA Study Week on Instrumentation for High Luminosity Hadron Colliders, held in Barcelona, Spain, September 14-21, 1989.
[7] D. Zilzinger et al. "The Helios Uranium Liquid Argon Calorimeter." In preparation, CERN, 1989.
[8] D.A.Landis, R.S.Adachi, N.W.Madden and F.S.Goulding. IEEE Transactions in Nuclear Science, Vol. NS-29, No. 1, February, 1982. p573.

N-10-90.FAX

Electrostatic Transformer Performances :

Shower Simulation

J. Colas

Summary : The electrostatic transformer idea (EST) has been developed to match the large capacitance signal towers of liquid ionization calorimeters to relatively low capacitance, low noise preamplifiers. The intrinsically fast internal impedance transformation by the EST preserves the fast rise time required for effective calorimetry in the high rate environment of the SSC/LHC. Practical implementations of the EST idea, have the adverse effect of some charge delocalization : a signal may appear in a tower with no shower. However, summing over several towers recovers the true shower energy. Detailed Monte-Carlo shower simulations, both for electromagnetic and hadronic calorimeters, have been made and show that for not too high a transformer ratio, the charge delocalization effect is much smaller than the natural shower spread. The EST connection scheme looks very promising.

1. Electrostatic transformer.

1.1 Transformer matching

In liquid ionization sampling calorimetry the charge is collected using high voltage across uniform sensitive gaps of liquid. These alternate with uniform plates of high Z absorber. The most significant limitations of the technology derive from the large source capacitance coupled with an intrinsically small ionization signal. The SSC/LHC needs for both fast signal response and excellent energy resolution are especially challenging because the frequent sampling needed for good energy resolution tends to require larger capacitance. 10 nF is typical for hadronic towers. Unless this is reduced, the preamp impedance as well as the inductances associated with cabling, feedthroughs and other connectors can limit significantly the charge transfer time. Larger capacitance also means more noise. To limit the power and cost of the electronics, the tower capacitance must also be minimized.

Alternative designs for a calorimeter tower are shown schematically in figure 1. In both cases the absorbing electrodes are separated by liquid sensitive gaps. Ionization electrons produced by shower particles are collected with the help of a large electric field (≈ 20 KV/cm). Figure 1a shows the traditional means of capacitance matching with an external ferrite-core transformer (FCT) [1]; within the tower all the signal gaps are in parallel. Figure 1b shows an alternative in which subsets of gaps within the tower are in series. As seen from the preamplifier, this performs an impedance transformation like that of the FCT and we called it electrostatic transformer (EST) [2, 3]. The similarity between the turns ratio of an FCT and the number of gaps in series of an EST is such that this last number has been dubbed "transformer ratio".

As an example of the use of an EST, a tower with 40 gaps of 200pF each has a total capacitance of 8 nF if all gaps are connected in parallel, but only 80 pF if there are 4 sets of 10 gaps each in series.

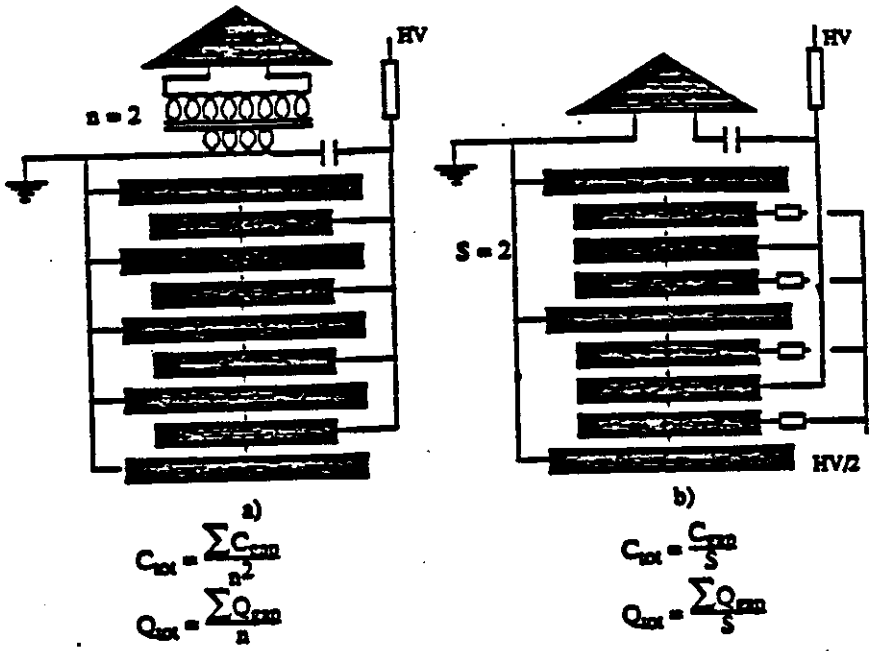

Equivalence between a ferrite transformer and an EST

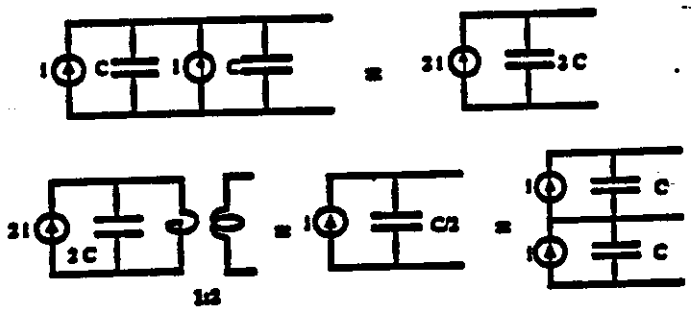

Figure 1. Comparison of the parallel (FCT) and series (EST) connection of several gaps. In the parallel case, the equivalent current source is the sum of the current in all (p) gaps. The total capacitance seen by the preamplifier is the sum of the capacitances of all gaps. A ferrite transformer of turn ratio n transforms this into a current <I> and a capacitance C/n. In the series connection, the equivalent current source is the average of the gap currents <I>. The capacitance seen by the preamplifier is the gap capacitance divided by the number of gaps in series (s in total) C/s. This smaller tower capacitance allows a faster readout. Note, that in both cases, energy conservation implies that the same signal to noise ratio is achievable.

1.2 Electrical performances of practical devices.

To study the electrical properties of the EST two aluminium models were built and tested in Berkeley [3,4]. The calorimeter stack consisted of nine towers (figure 2). The first model had only 10 gaps, the depth of second one was increased to 40 gaps. The gap thickness was 2mm. The absorber plates were mocked up by aluminium plates ≈ 1cm thick, with a transverse dimension of ≈ 15 x 15 cm^2. The separation between adjacent towers was varied between ≈ 3 and ≈ 8 mm. Electrical connections were varied too, to change the number of gaps in series, keeping the total number of gaps fixed. Charge was injected in one gap of the central tower. The source current waveform was triangular, of total length 100 ns and rise time less than 10 ns .

EST Aluminium model

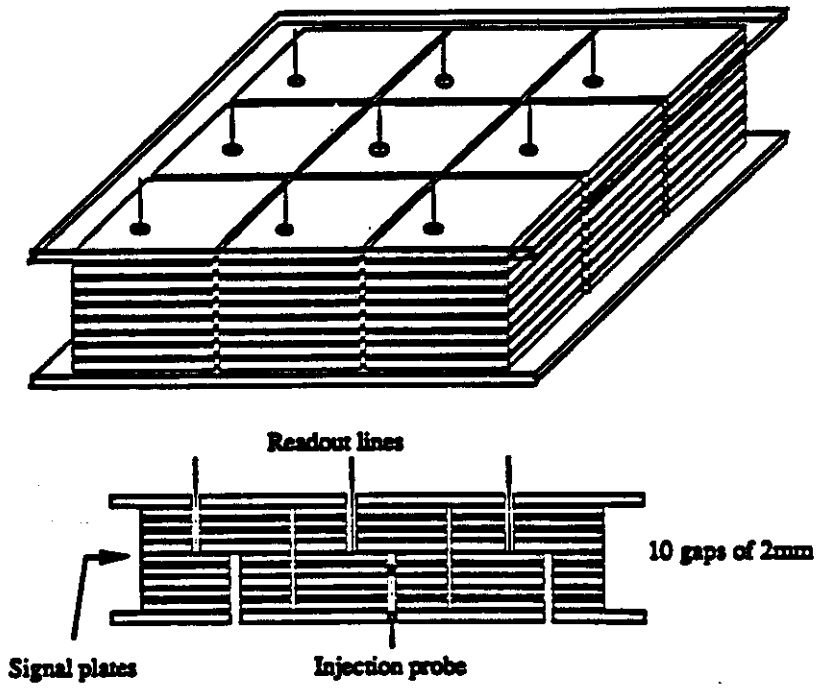

Figure 2 : Aluminium model to study the EST pulse properties. The set-up consists of nine towers. Each tower is made up of two parallel sets of gaps; each set with 1 to 5 gaps. Aluminium tiles are 6"x6" in area and 3/8" thick; gap size is fixed at 2mm; tower spacing can be varied from 1/16" to 1/2" to study the influence of the coupling capacitance.

Measurements were done on the central tower and one of its nearest neighbor. Examples of shapes observed on the central tower and side towers when all gaps or a single gap are excited are shown on figure 3. Even pulsing the central tower alone, signals are observed on the side towers; capacitive coupling between adjacent tiles spreads the signal over several towers.

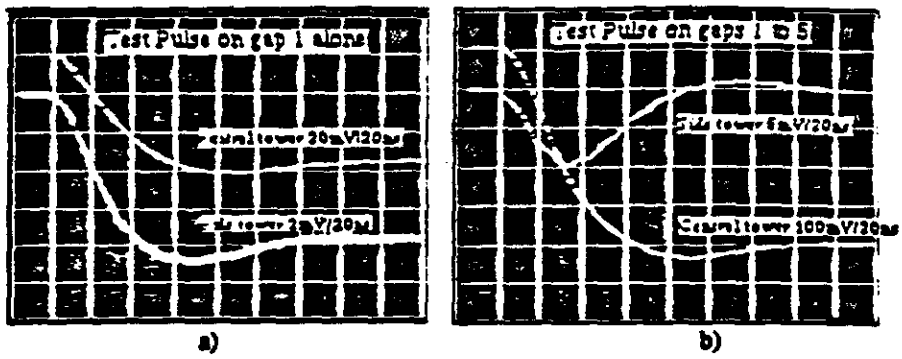

Figure 3. Preamp output pulses of central and side towers when a test pulse with a 100 ns drift time is fed into the structure. Transformer ratio is 5, and tower are spaced by 1/8". In a) gap 1 only is pulsed; in b) all gaps 1 to 5 are pulsed together.

With both calorimeter stacks good quantitative agreements were found between measurements and the predictions of the electrical circuit shown in figure 4 where the side towers are merged into one chain of capacitances capacitively coupled to the central tower.

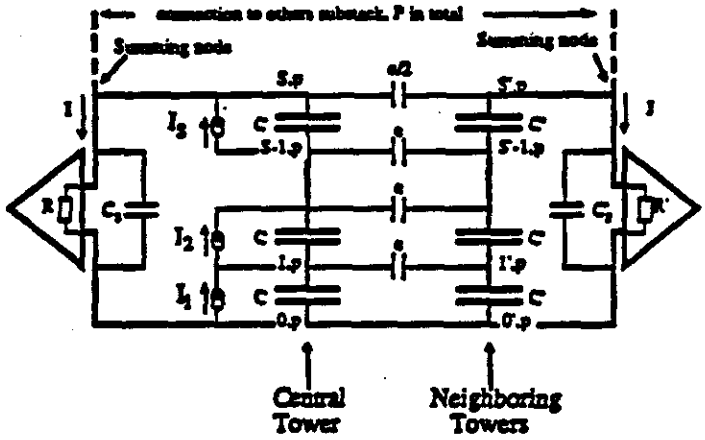

Figure 4. Equivalent electrical circuit of an EST

Electrical analysis of the circuit of figure 4 with N gaps connected in P parallel sets of S gaps in series, is described in reference 5. A gap is identified by two indices m and p. m the "serial gap #" describes the gap position in the series connection. m=1 is the gap closest to ground. p $1 \le p \le P$ identifies the parallel set. The main results of this analysis are :

1) For a source charge $Q_{m,p}$ deposited at time t=0 in gap [m,p], the sum over all tower signals is :

$$(Q_{m,p}/S)\,[1 - e^{-t/\tau}]$$

where $\tau = RCN / S^2 + RC_p$.

Compared to the parallel case, the signal is reduced by S but is delivered on a higher impedance with a much faster rise time ($1/S^2$). This does not depend on the gap in which the charge is deposited and so the signal summed over all towers will be exactly proportional to the deposited energy, as in the parallel case.

ii) For a source charge $Q_{m,p}$ deposited at time t=0 in gap [m,p], the proportion of crosstalk signal which appears on the side towers is proportional to the ratio of the coupling capacitance c to the gap capacitance C. In addition, crosstalk is made of two terms.
The first one χ_1 is a transient, also present in the parallel connection scheme and which does not depends on the gap number. It is clearly visible in figure 3. More specifically :

$$\chi_1 = \frac{c}{2C}\frac{PC/S}{C_s+PC/S}\frac{\tau}{\tau'-\tau}\left[e^{-t/\tau'} - e^{-t/\tau}\right]\sum_{k=1}^{S} F_{S-k}$$

with $\tau' = RC_s + RPC/E_S$.
The numbers F_{S-k} and E_S depend on the ratio c/C and are tabulated in [5]. To first order in c/C one gets :

$$F_{S-m} = \frac{S^2-m^2+m}{S} \; ; \; \sum_{k=1}^{S} F_{S-k} = \frac{2S^2+1}{3} \quad \text{and} \quad E_S = S \quad \text{i.e. } \tau' = \tau$$

This component reaches its maximum for $t_{max} = \tau$ and vanishes for time large compared to τ. In the following we ignore it for simplicity.

The second one does not tends to zero at large time as seen on figure 3 again. However as explicit shown on the formula below, it is identically zero if the same charge is deposited in all the gaps connected in series. This is easy to understand as in this case there is no charge accumulation on the nodes of the capacitance chain and hence no voltage variation, i.e., no crosstalk.

$$\chi_2(m,p) = \frac{c}{2C}\left(1-e^{-t/\tau'}\right)\left[S\,F_{S-m} - \sum_{k=1}^{S} F_{S-k}\right]$$

1.3 Gap efficiency and charge delocalisation

From i) and ii) above, the signal in the central tower will depend on the gap m,p in which a charge is deposited, and one can define a gap efficiency ε_m such that the signal in the central tower is

$$\Psi = \sum_{p=1}^{P}\sum_{m=1}^{S} \varepsilon_m \, Q_m/S$$

The signal in the neighboring towers is

$$\chi_t = \sum_{p=1}^{P}\sum_{m=1}^{S} (1-\varepsilon_m) \, Q_m/S$$

According to ii) at large time, the gap efficiency is,

$$\varepsilon_m = 1 - \frac{c}{2C}\left[S F_{S-m} - \sum_{k=1}^{S} F_{S-k} \right].$$

ε_m equal one means that all the charge appears in the central tower and that there is no crosstalk. ε_m less than one means that some part of the signal disappears from the central tower to appear on the side towers. For ε_m greater than one there is a negative crosstalk contribution on the neighboring channels which enhances the central signal. The table below gives gap efficiencies for a typical coupling ratio c/C of 0.12 [5].

Gap efficiencies versus transformer ratio for a coupling ratio c/C = 0.12										
1	1.000									
2	0.944	1.056								
4	0.768	0.853	1.036	1.344						
8	0.433	0.468	0.543	0.669	0.866	1.163	1.604	2.255		
10	0.334	0.355	0.398	0.471	0.585	0.756	1.011	1.388	1.943	2.759

To get a feeling of the importance of the charge delocalization effect induced by this non uniform gap efficiency, let us consider a model where in all gaps, the charge is the same on average Q, but fluctuates independently in each gap. The error introduced by the non uniformity in the gap collection efficiency is zero but gives rise to an additional fluctuation on the energy detected by the central tower :

$$\frac{\sigma(v)}{v} = \frac{\sigma(Q)}{Q} \times \frac{\sqrt{\sum_{m=1}^{S} (\varepsilon_m 2 - 1)}}{S}$$

The energy which is not detected in the central tower will be seen in the side towers. The delocalization coefficient (last factor on the right) is not large for the transformer ratios shown below. For instance, with a gap to gap fluctuation $\frac{\sigma(Q)}{Q} = 0.2$ and a transformer ratio of 4, the signal which appears on the side towers is zero on average with an RMS fluctuation of = 2% of the signal in the central tower.

Transformer ratio	1	2	4	6	8	10
$\frac{\sqrt{\sum_{m=1}^{S} (\varepsilon_m 2 - 1)}}{S}$	0	0.039	0.111	0.170	0.213	0.242

To summarize, summing over all towers will always give the correct energy. However, if the shower fluctuates such that the charges deposited in the gaps connected in series are very different from each other, the signal collected in the central tower may be different from the true energy deposited in that tower, the difference appearing in the adjacent channels.

The questions to be answered are then :

i) How large are shower fluctuations from one gap to the next ?

ii) How much do they affect the tower signal ?

iii) How important is the energy spread induced by these fluctuations ?

2. Shower simulation.

2.1 Calorimeter geometry

To quantify the charge delocalization effect described above, two calorimeter models have been set-up, one for hadronic showers and a second one for electromagnetic showers. Both consists of a 7 x 7 array of square towers. The detection gap is 2mm thick and filled with TMP. Lead is used as an absorber with a 8 mm thickness for the hadronic model, reduced to 2 mm in the electromagnetic case.

The hadronic tower size is 15 x 15 cm^2, including a 4 mm spacing between towers; the actual lead tile transverse dimension is thus 14.6 x 14.6 cm^2. 200 layers in depth provide for ≈ 10 interaction lengths. These dimensions would give a granularity $\Delta\eta x\Delta\phi$ of 0.06x0.06 for a calorimeter with an average distance from the collision point of 2.5 m.The gap capacitance is 190 pF and the coupling capacitance to the four nearest neighboring towers 21 pF. The corresponding gap efficiencies as a function of the transformer ratio according to [5] are shown below:

Transformer ratio	Efficiency in each gap									
1	1.0									
2	0.949	1.051								
4	0.783	0.863	1.034	1.319						
10	0.352	0.373	0.417	0.491	0.606	0.775	1.024	1.385	1.909	2.667

The electromagnetic tower size is 5 x 5 cm^2, including a 2 mm spacing between towers; the actual lead tile transverse dimension is thus 4.8 x 4.8 cm^2. With these dimensions, 99% of the shower energy is contained in a 3 x3 array. With 100 layers in depth the electromagnetic calorimeter has a total thickness of close to 35 radiation lengths. For a calorimeter at an average distance from the collision point of 1.7 m These dimensions would give a granularity $\Delta\eta x\Delta\phi$ of 0.03x0.03. The gap capacitance is 20.5 pF and the coupling capacitance to the four side towers 3.4 pF. The corresponding gap efficiencies for different readout connection schemes are :

Transformer ratio	Efficiency in each gap							
1	1.0							
2	0.925	1.075						
4	0.704	0.809	1.040	1.447				
8	0.361	0.394	0.468	0.597	0.810	1.149	1.687	2.534

2.2 Shower simulation

The tracking package GEANT with the codes EGS and Gheisha have been used to simulate the showering process through these two calorimeter models. γ were tracked down to 100 keV, electrons, protons and neutrons down to 1 MeV. The electromagnetic shower package EGS has been checked many times against experimental results and its predictions found to be very accurate. This is not yet the case for the hadronic code Gheisha which has to simulate

numerous low energy nuclear effects. Although these imperfections affect detailed predictions such as the e/π ratio or the energy resolution of the calorimeter, it is not expected that they will influence the results of this study.

20 GeV electrons were tracked through the electromagnetic calorimeter model. When the beam aims normally at the center of the middle tower, a negligible amount of energy escapes detection. 90% of the shower energy is contained in this central tower and as already mentioned above 99% in a 3 x 3 array. If the cell size is reduced to 3 x 3 cm^2 the corresponding containment figures become 82% and 96%, respectively. The energy resolution is $\frac{9.5\%}{\sqrt{E}}$

50 GeV pions were tracked through the hadronic calorimeter model. For normal incidence angle in the center of the calorimeter, 2.9% of energy escapes through the sides of the calorimeter, 0.2% through the back and 1.3% is lost through the front face. Normalized to the energy detected in the calorimeter, 73% of this energy is contained in the central tower, 93% in a 3x3 array, rising to 98% for a 5x5 array.

2.3 Readout structure

For each calorimeter, several readout structures have been tried. To allow detailed studies, the hadronic calorimeter has been subdivided in 5 samplings of 40 sensitive gaps each. The electromagnetic calorimeter was cut in four samplings of 8,32,32 and 24 layers i.e. = 3, 12, 12 and 8 X^0.

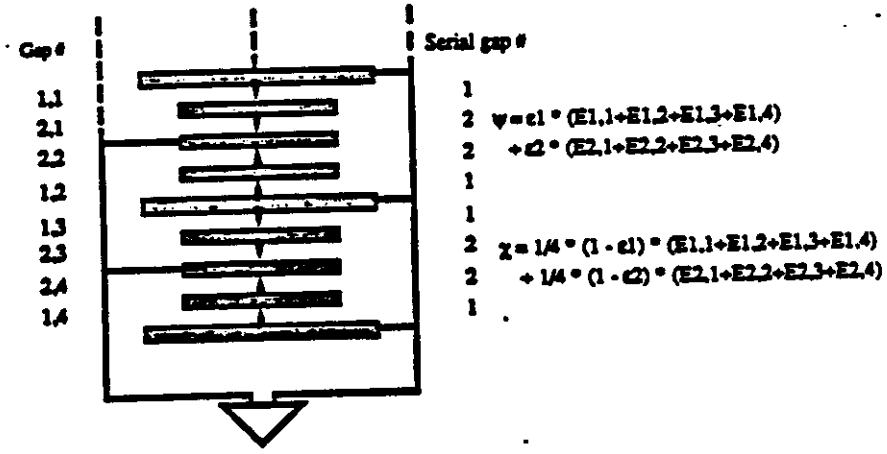

Figure 5: Example of a readout structure used in the simulation. This picture defines the serial gap number and shows how the readout signal is obtained from the energy deposition in each gap, ψ in the central tower and χ in each of its four nearest neighbors

Inside each sampling, gaps are either connected in parallel (i.e. the energy in all gaps is summed to give the output signal), or connected in a mixed series parallel scheme as shown in figure 5. The signal tile is in the middle of a double set of gaps connected in series. The number of gaps in series S is varied from 1 to 8 in the electromagnetic case and up to 20 for the hadronic calorimeter. The case S=1 corresponds to the standard parallel readout scheme. We define the energy in each serial gap m, $1 \le m \le S$, to be the sum of the energies deposited in each m^{th} gaps of the p parallel sets of series gaps (see figure 5); i.e. according to the gap labelling defined in 1.2, we sum over the parallel index p. This energy is then used to compute the signal from the

tower where the energy deposition occured and of its neighbors, according to the gap efficiency as discussed in 1.3 above. In this simulation, each tower has four closest neighbors which share an edge, and the crosstalk signal is divided up equally between them.

In this first analysis, possible effects due to finite electron drift time in liquid have been neglected.

3. Results.

Most of the results presented below have been obtained with the beam impinging normally at the center of the central tower. Other coordinates for the incident beam gave similar results. So unless otherwise specified, results with a centered beam are reported.

A detailed analysis, sampling by sampling has also been done. All these results are consistent with those of the calorimeter considered as a whole; the lamerare reported below.

3.1 Fluctuations between gaps

As discussed in 1 the energy spread due to the lateral tile coupling is related to the fluctuation in the energy deposition from gap to gap. To get a feeling for the magnitude of this fluctuation let us consider a readout structure where each calorimeter sampling consists of sets of 4 gaps in series. Inside each sampling, we sum over over all gaps with the same serial index m to obtain, as explained in 2.3, the energy deposited in each of the serial gaps; we then compute for each event the average energy deposition in a serial gap and the variation around this mean value.

Figure 6 shows these fluctuations normalized to the average energy deposition in a gap and summed over all calorimeter samplings. Each entry in the histogram is weighted by the average energy in a gap to take into account the proportionality between the energy deposition and the output signal.

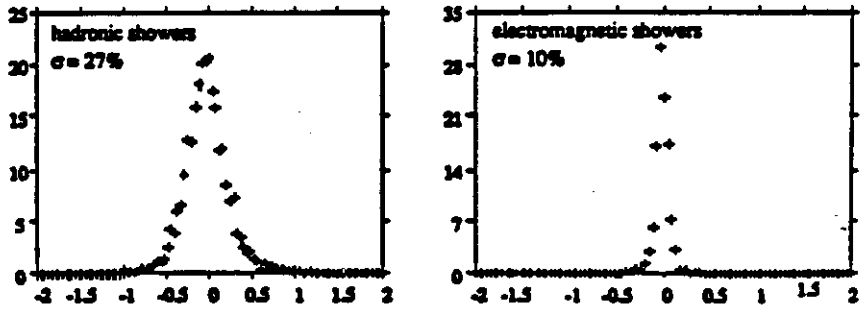

Figure 6: Gap to gap energy variation in a structure with four gaps in series. The energy variation is normalized to the average energy in a gap.

Electromagnetic showers do not fluctuate much even on a distance as large as 4 gaps. This small fluctuation is better understood if ones realize that in sampling 2 (32 gaps) of our model, for instance, each serial gap includes 8 gaps; this effectively reduces the apparent gap to gap fluctuations. We can thus already expect, following the results obtained in 1.3, that for these showers the charge delocalization effect of the EST will be small.

Predictably, we find that hadronic showers fluctuate more. This is partly due to the thicker sampling ratio used in the hadronic calorimeter.

Detailed numbers for each sampling are given in the table below, which also shows the fraction of the shower energy deposited in the central tower. As expected, samplings with little energy fluctuate more.

Electromagnetic showers					
Sampling #	all	1	2	3	4
Energy % in samplings of the central tower	90.7	4.0	79.8	6.7	0.2
Energy fluctuation RMS (%)	10.5	31.9	5.9	19.1	—

Hadronic showers						
Sampling #	all	1	2	3	4	5
Energy % in samplings of the central tower	73.6	47.5	21.3	4.1	0.7	0.05
Energy fluctuation RMS (%)	27.3	22.2	30.6	38.9	43.1	—

3.2 Signal fluctuation in the central tower

The energy gap fluctuation described in 3.1 above, induces through the imperfection in the EST action, a variation in the central tower signal. Let's take as a reference the signal delivered by the central tower with all gaps connected in parallel. Then, event by event, we can compute the normalized signal variation in that tower if we change the electrical connection from parallel to a mixed series parallel scheme. Two examples of distribution of this quantity for rather large transformer ratios are shown in figure 7.

Table 2 below gives for various transformer ratios, the central values and RMS of these distributions . The central values are close to zero which we expect, as on the average nearly the same energy is deposited in each gap of the series. In addition, for not too large transformer ratios, this additional fluctuation introduced by the EST action is smaller or comparable to the natural shower fluctuation itself. In this table, this is defined as the event by event fluctuation of the energy fraction in the central tower. The fluctuation in the energy deposition typical of sampling calorimeters is also given. Only for the very large transformer ratio of 20, which has been tried on hadronic showers, is the signal from the central tile poorly correlated with the energy deposition.

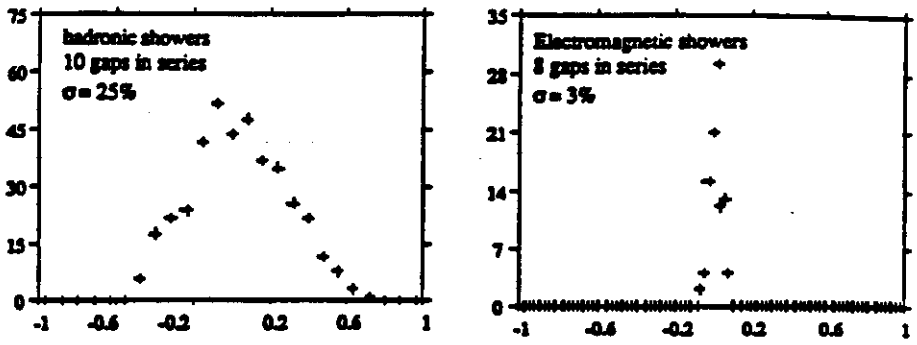

Figure 7: Normalized central tower signal variation with respect to the parallel connection scheme.

Electromagnetic Showers Variation in the signal from the central tower with respect to the energy deposited in the same tower			
Transformer rapo	2	4	8
<δE/E>	0	0	.026
δE/E RMS	.002	.009	.031
Natural Shower Fluctuation	.009		
Sampling fluctuation	.021		

Hadronic Showers Variation in the signal from the central tower with respect to the energy deposited in the central tower				
Transformer rapo	2	4	10	20
<δE/E>	0	0	.037	.057
δE/E RMS	.005	.026	.248	.58
Natural Shower Fluctuation	.094			
Sampling fluctuation	.100			

3.3 Shower energy spread

We do expect, according to the EST properties recalled in 1.2, that if we sum over several neighboring towers the additionnal fluctuation introduced by the EST action and described in 3.2 above will be greatly reduced. Table 3 compares the transverse energy containment inside arrays of increasing sizes: 1x1, 3x3 , 5x5 and 7x7. This is shown for several calorimeter structures where the number of gaps in series varies from 1 to 8 in the electromagnetic case and up to 20 in the hadronic case. The case S=1 where all gaps are connected in parallel is shown as a reference. For each configuration this table gives the average energy containment (<>) and also the RMS fluctuation around this mean value (σ).

Transformer ratio		Electromagnetic shower containment inside larger and larger arrays			
		1x1	3x3	5x5	7x7
S=1	<>	90.74	98.75	99.75	100.
	σ	.9	.4	.2	0
S=2	<>	90.76	98.75	99.75	100
	σ	.9	.4	.2	0
S=4	<>	90.81	98.74	99.75	100
	σ	1.3	.4	.2	0
S=8	<>	93.16	98.78	99.74	100
	σ	2.8	.5	.2	0

Transformer ratio		Hadronic shower containment inside larger and larger arrays			
		1x1	3x3	5x5	7x7
S=1	<>	73.5	93.0	98.4	100.
	σ	9.4	3.5	1.2	0
S=2	<>	73.6	93.0	98.4	100
	σ	9.4	3.5	1.2	0
S=4	<>	73.54	93.03	98.4	100
	σ	9.5	3.5	1.2	0
S=10	<>	76.5	93.0	98.4	100
	σ	22.6	3.7	1.2	0
S=20	<>	78.5	93.2	98.4	100
	σ	46.7	5.0	1.5	0

These numbers show that, as already discussed in 3.2, the average energy containment is insensitive to the transformer ratio up to very high values; the fluctuation around the mean is more sensitive. Again, we find that for the very high transformer ratio of 20 the signal coming out of the central tower varies widely around its mean value and is practically of no use. However, as soon as one sums over several towers, an energy resolution similar to the one obtained for the parallel case is recovered even in this extreme case.

3.4 Shower energy profile

If we want to discriminate against two close by showers, widening of the energy profile by EST action is not a very desirable feature. Figure 8 compares electromagnetic shower energy profile along one tranverse dimension for the parallel connection scheme and for a transformer ratio of 4, both when the beam impinges at the center of the tower and when it is close to an edge (1mm). The differences are hardly noticeable.

For completeness figure 9 gives for various transformer ratios the average shower width and the RMS indicated as error bars. More precisely, the signals from calorimeter array are summed along one dimension (y); then for each event and for each transformer ratio, the quantities

$$\langle x \rangle = \frac{\sum_{k=1}^{n} x_k E_k}{\sum_{k=1}^{n} E_k} \quad \text{and} \quad w^2 = \frac{\sum_{k=1}^{n} (x_k - \langle x \rangle)^2 E_k}{\sum_{k=1}^{n} E_k}$$

SDC-90-00071

SDC
SOLENOIDAL DETECTOR NOTES

ELECTRONIC SIGNAL TO NOISE RATIO FOR LA, TMP, AND TMS

W. Wenzel

August 9, 1990

Electronic Signal to Noise Ratio for LA, TMP, and TMS

We follow the formulation by Jacques Colas (LBL-27328, Alabama Workshop, 3/89):

$$S/N = \beta\, I_{max}\, T_{eff}\, \mathrm{sqrt}(T_m L/A) = (\beta B q g/2)\, \mathrm{sqrt}(T_m L/A)$$

where β=4.3 for LA and 3.8 for TMP or TMS, I_{max} is the initial current in ke/μsec in the triangular pulse of length T_d=drift time. T_m is the measurement time; we use the shaper response shown in the left figure below. L(m) and A(sq m) are the sum in depth of gap widths, and the area of each gap, respectively. T_{eff} is the effective time during which the shaper collects charge. Using the drift velocity v_d(cm/μsec)=g/T_d=I_{max}/q, N may be expressed also in terms of the gap width g(cm), the linear charge density q(ke/cm), and a 'ballistic' factor:

$$B = 2T_{eff}/T_d = (1.27T_m/T_d)[1-\exp(-T_d/1.27T_m)] \le 1,$$

which measures the effective fractional charge utilization. A small value for B implies a greater relative sensitvity to pile-up. Greater rejection of pile-up could be achieved, with a factor sqrt(3) increase in noise, using the fast bipolar shaping function shown at the right below.

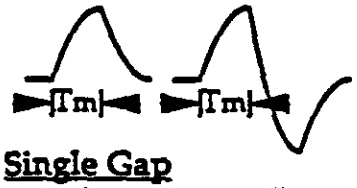

Single Gap

At the right we show S/N and B for mips in one gap: i.e., we take:

L(m)=0.01g(cm)

A=0.01 sq m.

For LA

- E=V/g is taken to be 10kV/cm; the performance is not sensitive to this value.
- S/N ∝ Tm sqrt(gTm)
- B is generally small for large g.

For TMP and TMS

- Both Td and q are functions of E. We use V = 5 or 10 kV. The maximum voltage is assumed to be set by the feedthroughs and insulators rather than the liquid gap width.
- For both S/N and B the 10kV curves lie above those for 5kV.
- Trade-off of I_{max} and capacitance produces a peak in S/N vs g with:
- $(S/N)_{max} \propto VT_m$
- $g_{max} \propto \mathrm{sqrt}(VT_m)$.
- $B(g_{max}) \approx 0.5$.
- $S/N_{TMS}\,/\,S/N_{TMP} \approx 2$

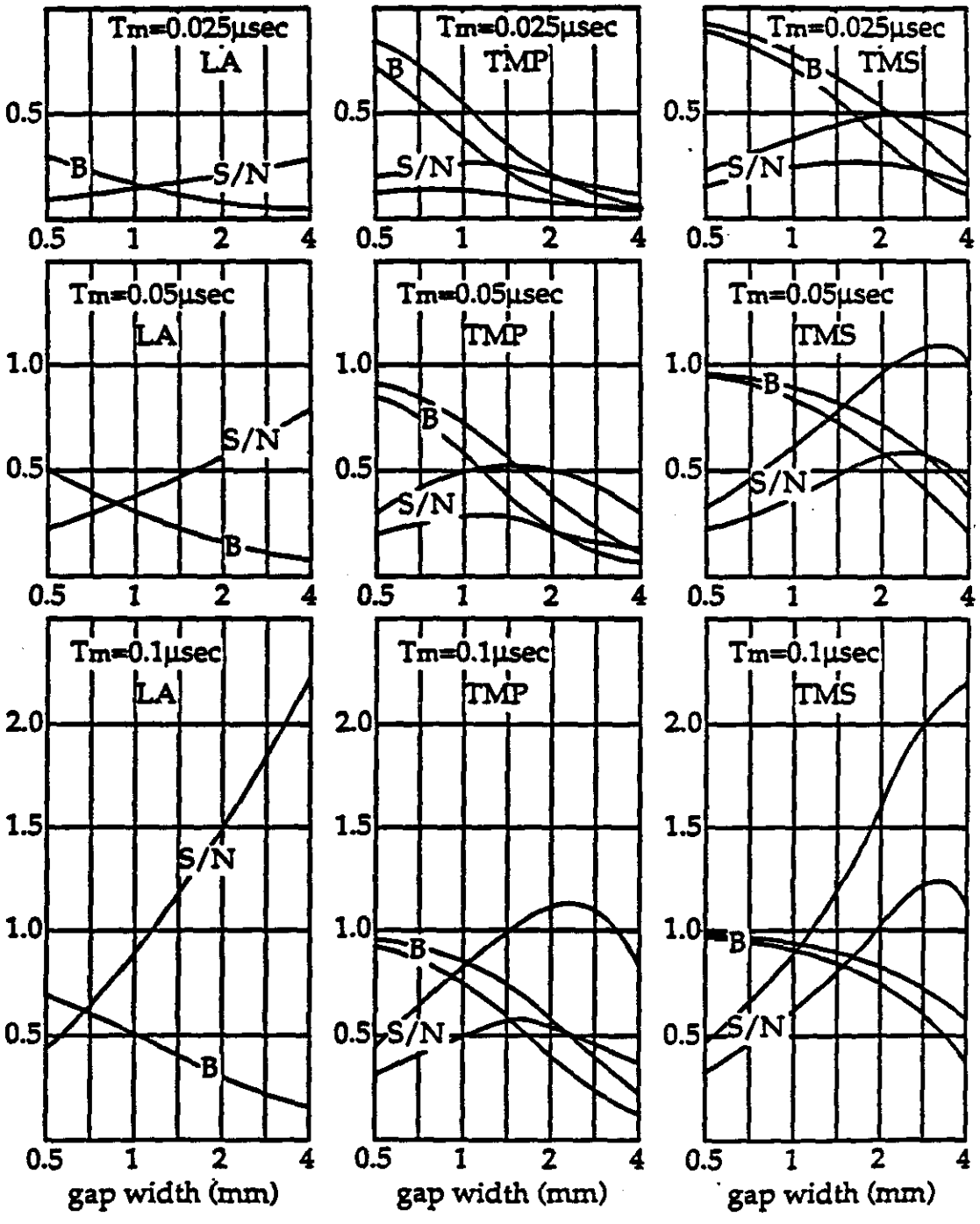

In the calculations above we have ignored the implications of the g-dependence of calorimeter density, absorber thickness, relative gap tolerances, etc, each of which affects the resolution. As an example, the total depth of liquid may be limited to achieve e/h compensation or to maintain a large average calorimeter density. Then larger gap width implies poorer sampling and resolution.

Fixed Liquid Depth

If the total liquid depth ($L=\Sigma g$) is specified, there is a trade-off between gap width and gap number. e.g., L=0.1m represents 50 gaps of 2mm width or 100 gaps of 1mm width, etc. Here we consider specifically S/N for a liter of liquid, i.e., with:

L=0.1 m, A=0.01 sq m.

Then each S/N is obtained from that calculated previously by multiplying by sqrt[10/g(cm)]. B(g) is unchanged. Below are calculated values of S/N and B for the same liquids and values of Tm used in the single gap example above.

- Compared with the single gap solution, S/N is now maximized at smaller gaps, where B is larger.
- For most cases, S/N>1; hence mips are detectable in this tower section.

For LA
- B values are small, but S/N is only moderately, if at all, dependent on g; a small gap minimizes pile-up.

For TMP, TMS
- S/N peaks are shifted to smaller gaps.
- $(S/N)_{max} \propto Tm$; the dependence on V is slightly less than linear.
- $g_{max} \propto \sqrt{Tm}$; the dependence on V is slightly less than sqrt.
- $B(g_{max}) \approx 0.7\text{-}0.8$ - pile-up is small -
- At each V and Tm, the peak value of S/N for TMS is sqrt(2) times larger than for TMP.
- At Tm=0.05μsec, the S/N peaks are at:
  g ≈ 1 mm for TMP
  g ≈ 2 mm for TMS